# REPORT DOCUMENTATION PAGE

Public reporting burden for this collection of information is estimated to average 1 hour per response, including the time for reviewing instructions, searching existing data sources, gathering and maintaining the data needed, and completing and reviewing the collection of information. Send comments regarding this burden estimate or any other aspect of this collection of information, including suggestions for reducing this burden, to Washington Headquarters Services, Directorate for Information Operations and Reports, 1215 Jefferson Davis Highway, Suite 1204, Arlington, VA 22202-4302, and to the Office of Management and Budget, Paperwork Reduction Project (0704-0188), Washington, DC 20503.

| 1. AGENCY USE ONLY (Leave blank) | 2. REPORT DATE | 3. REPORT TYPE AND DATES COVERED |
|---|---|---|
| | | FINAL |

| 4. TITLE AND SUBTITLE | 5. FUNDING NUMBERS |
|---|---|
| Ion Clusters and Exotic Plasma States | 61102F <br> 2301/ES |

**6. AUTHOR(S)**

V. Nardi, J.S. Brzosko, C. Powell

| 7. PERFORMING ORGANIZATION NAME(S) AND ADDRESS(ES) | 8. PERFORMING ORGANIZATION REPORT NUMBER |
|---|---|
| Stevens Institute of Technology | AFOSR-TR- 95 0150 |

| 9. SPONSORING/MONITORING AGENCY NAME(S) AND ADDRESS(ES) | 10. SPONSORING/MONITORING AGENCY REPORT NUMBER |
|---|---|
| AFOSR/NE <br> 110 Duncan Avenue Suite B115 <br> Bolling AFB DC 20332-0001 | AFOSR-91-0158 |

DTIC
SELECTED
MAR 27 1995
G

**11. SUPPLEMENTARY NOTES**

| 12a. DISTRIBUTION/AVAILABILITY STATEMENT | 12b. DISTRIBUTION CODE |
|---|---|
| APPROVED FOR PUBLIC RELEASE: DISTRIBUTION UNLIMITED | |

**13. ABSTRACT (Maximum 200 words)**

19950323 145

SEE FINAL REPORT ABSTRACT

| 14. SUBJECT TERMS | | | 15. NUMBER OF PAGES |
|---|---|---|---|
| | | | 16. PRICE CODE |

| 17. SECURITY CLASSIFICATION OF REPORT | 18. SECURITY CLASSIFICATION OF THIS PAGE | 19. SECURITY CLASSIFICATION OF ABSTRACT | 20. LIMITATION OF ABSTRACT |
|---|---|---|---|
| UNCLASSIFIED | UNCLASSIFIED | UNCLASSIFIED | UNCLASSIFIED |
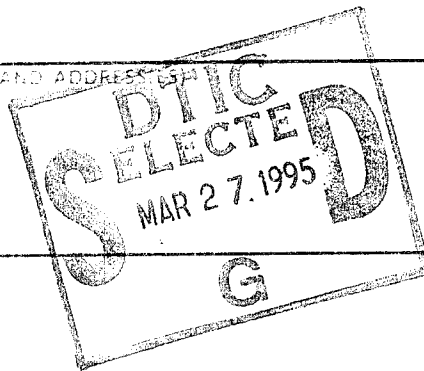
# STEVENS

Stevens Institute of Technology ◆ Castle Point on the Hudson ◆ Hoboken, New Jersey 07030

AFOSR-TR- 95 0750

# ION CLUSTERS AND EXOTIC PLASMA STATES

Final Technical Report Prepared for

Air Force Office of Scientific Research

Bolling AFB, DC 20332-6448

V. Nardi, J. S. Brzosko, C. Powell

February 28, 1994

| Accesion For | |
|---|---|
| NTIS CRA&I | ☒ |
| DTIC TAB | ☐ |
| Unannounced | ☐ |
| Justification | |

By _____
Distribution /

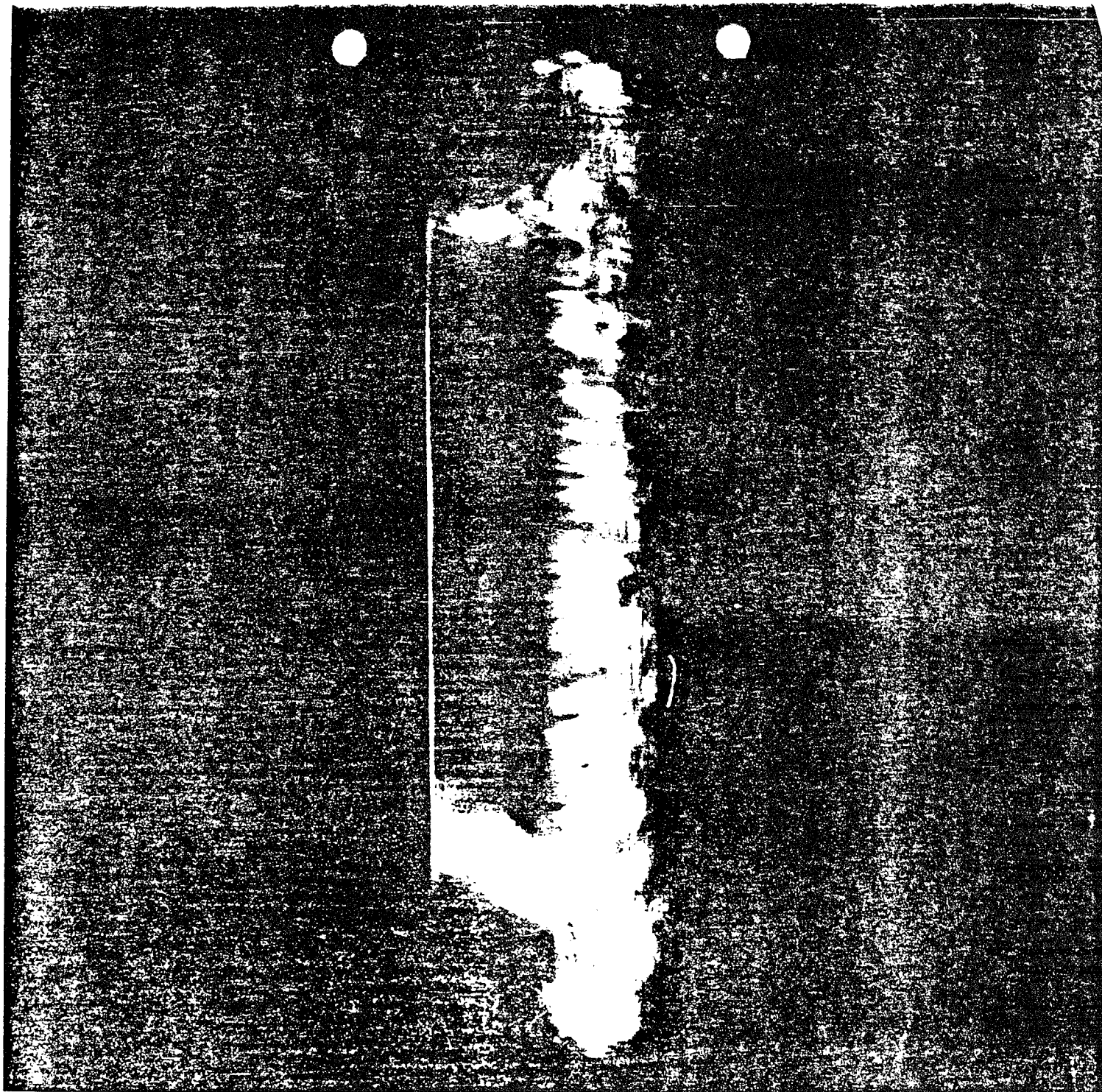| Availability Codes | |
|---|---|
| Dist | Avail and / or. Special |
| A-1 | |

Final Technical Report

Contract No AFOSR-91-0158

Period Covered 1 February 1991 - 31 January 1994

⊗ Integrating Knowledge to Create Leaders

Schlieren image of the radially imploding current sheet. The exposure duration (> 40 ns) provides (via time integration of the image ) critical information on the non uniform velocity of the current sheet, specifically, on oscillations of the velocity of period > 15 ns, as reported in the publication No 4 of Chapter 5

This report contains 11 pages with Figures and captions not numbered, in addition to the 27
numbered pages + cover.

# ION CLUSTERS AND EXOTIC PLASMA STATES

## Summary

The completed major parts of the three year program are (1) upgrading of the plasma focus machines of the Stevens Tech laboratory to higher powering energy levels $W_1 > 20$ kJ and $W_2 > 100$ kJ, (2) test of the scaling laws relating fluence and spectral characteristics of the ion cluster and supercluster emission to W, (3) clarification of the leading physical processes which are characteristics of the plasma source of ion clusters and of superclusters with mass/charge ratios $> 10^{12}$ a.u., and data acquisition and evaluation with new methods, specifically addressing ion clusters and related exotic plasma states.

The source of ion clusters and of superclusters, as well as the source emission, are examples of exotic plasma states. These include, but are not limited to, states of self-field-dominated plasma where the self-field energy is of the same order of magnitude of the particle kinetic energy. The particle motion is self-organized from the $<10^{-5}$ cm to the $>2$ cm scale, with the bulk of the kinetic energy stored in the organized motion exceeding the thermal energy.

**Index**

# Introduction

The upgrading to higher energy levels W of the capacitor bank and switching components of at least one of our plasma focus (PF) machines was a necessary step for testing some of the basic characteristics of the self-field-dominated plasma as functions of W. As an addition to all previous diagnostics, which includes Thomson parabola spectrometers with time resolution up to 1 ns, ion energy magnetic analyzers with energy resolution dE/E better than 0.5% in the interval 1 MeV < E < 5 MeV, we have substantially improved the ion and ion cluster target diagnostics by exploiting a newly-observed effect on the imaging formation process of impacting plasma components. This effect involves the strong dependence of the ion track density $v$ (cm$^{-2}$) which forms the image of the impacting plasma, on the spacing $0 < \Delta < 0.5$ mm between the ion filter and the CR-39 target.

New results, which we consider more relevant than others for evaluating the completed project, are reported in the Chapters 1 to 5 of this report. Greater details on specialized topics are reported in Appendices I, II. The list of published papers ( Chapter 5 ) includes only the papers which were published or are accepted for publication with a specified publication date within 1994. Other submitted papers, some already accepted for publication but without a specified publication date, are not included in the publication list.

Several Visitors to the Stevens Tech laboratory from other Institutions and three Stevens Tech. Graduate students have effectively contributed to diagnostic procedures, to data acquisition and analysis and to the construction of new PF machines at higher W levels. This was possible because of the laboratory capability of independently and simultaneously operating at least four PF machines.

The laboratory facilities include. (a) A five module W > 100 kJ PF, with three modules fully completed and tested (b) A new design, mobile, W > 20 kJ PF, entirely built after the project start This unit is now routinely and successfully operated for testing the scaling laws of the ion and ion-cluster emission with W. (c) The three existing PF machines at energy levels 5 kJ < W < 10 kJ in operation in our laboratory at the starting time of this project, which now continue to operate in parallel with the new PF machines built during the project.

Among the Visitors, the laboratory hosted Dr. H. Kilic, of Ferrara University, Prof. C.M. Luo and Dr. J. Wang of Tsinghua University, Dr. K. Melzacki of KMC, Troy, NY. The Graduate students are D. Goldstein, L. Schneider, both supported by an AF-AASERT Grant, and H. Woo. A Senior Undergraduate student, R. Brzosko, did participate to the neutron emission measurements, in fulfillment of a Senior Research Project.

Some of the diagnostics methods were improved in the last stage of the project. One example is the Geiger counter systems for monitoring the $\beta^+$-decay of the radioactive nuclei from high-Z reactions in the plasma. A second example is the merging of a compact Thomson spectrometer with a particle-emission imaging system.

## 1. Upgraded Plasma Focus Machines With Powering Capacitor Bank of Energy > 20 kJ and W ≥ 100 kJ

All PF machines of the laboratory include a circular knife edge at the breech of the coaxial electrodes. This field distortion element (FDE) performs as a field emitter with the net effect of increasing the neutron yield per pulse, Y, from D + D reactions by a factor > 3, as compared to the Y values from the same machine, under identical conditions but without FDE. A second FDE-induced benefit is the decrease of the fluctuation of Y from discharge to discharge. The distribution of Y values becomes a gaussian with a full-width-at half-maximum (FWHM) $\simeq$ 20 to 25 % of the mean value $Y_{av}$ of Y over hundreds of discharges. The Y-fluctuation level is further reduced by decreasing the contamination of the filling gas with high-Z nuclei. The cylindric electrodes of all five PF machines have Mather's geometry.

The PF operation is usually carried out with a pure deuterium filling or with a substantial fraction of $D_2$ in the filling gas mixture. This is done because the neutron yield Y from D+D reactions provides an accurate, simple-to-obtain quantitative description of the quality of the pinch. The quality of the pinch is measured by the ratio of the energy transferred to the pinch to W. Optimization of a PF machine means here that the choice of electric and geometric parameters is such that for the chosen value of W, Y has its maximum value. Each PF machine is equipped with a Rogowski belt between the back plates supporting the electrodes at the breech to monitor the PF electrode current as a function of time.

### W > 100 kJ PF system
[This notation means that optimization conditions may not be met during operation at energy levels substantially below 100 kJ, e.g., by more than 35 %].

A PF (W > 100 kJ) with a five module capacitor bank, complete of power supply, vacuum systems, and discharge chamber with electrodes, was assembled with five pairs of copper plates 1 ft wide as power transmission lines. Each of the five modules was tested by using five field-distortion switches, with synthetic (culled) electrodes. The switches (Los Alamos and General Electric design) for this W > 100 kJ machine were built in our laboratory and tested at peak current levels above 140 kA for about 2,000 discharges of a 40 kJ pulse-forming network. Each flat current pulse had a duration of 10 μs before reversal. The initial switch-trigger system was suitable for triggering only two modules at a time. Each of the five modules had initially a nominal maximum energy of 40 kJ at 60 kV. During the present project, the following modifications were implemented. Each module was increased to store 100 kJ at 60 kV. The objective was to decrease the inductance of each module, and have a viable operation at a relatively-lower voltage. The layout of the newly-assembled system is shown in Fig.1.

This improvement was made possible by the new capacitor bank obtained from the Los Alamos National Laboratory with the vouching of the AFOSR and the initiative of the Program Manager, Dr. Robert J. Barker.

A second major improvement was the acquisition of a Maxwell-Laboratory-state-of-the-art trigger and switching system. This new unit, complete of 100-kV-multiple trigger generator with 10 outlets (see Appendix I description), master-100- kV trigger, and one Maxwell-Laboratories rail gap switch was purchased by a collaborating institution of the private sector (AES Dense Plasma Laboratories, Inc.) and given on loan to the Stevens Tech. laboratory.

The new trigger and switching system was applied to a new W > 20 kJ PF machine before transferring it to the W > 100 kJ PF system.. The objective was to test the scaling law relating the PF emission to W at a medium energy level, before committing our limited resources to the tests at the maximum energy level > 100 kJ.

## W > 20 kV PF system

[ This notation has the same meaning as above. Operations below ~ 35% of the indicated W value may become impaired. Operations up to W ~ 50 kJ are possibile with only minor changes ].

This unit utilizes two of the earlier modules of W > 100 kJ as capacitor bank. An effort was made to build this unit of compact design to achieve mobility. The system is assembled on a wheeled platform and can be moved by a single operator, without helping tools, from one area to another area of the laboratory. The layout is reported in Fig.1
The peak electrode current with the capacitor bank charged at 30 kV is ~ 1 MA.

An additional 10 kJ-Aerovox capacitor can be hosted easily in each of the two modules of this unit, in order to increase W by dW = 25 %, and to have suitable variations dC of the capacitance C, and dL of the inductance L of the powering system. Tests on the differential increment of the emission of ion and of ion clusters, with the variations dW, dC, dL and with the charging voltage V facilitate the discrimination of random fluctuations from more significant, sistematic variations of the emission.

The switching and triggering components can be moved from the W > 20 kJ-PF system to the W > 100 kJ PF system in a matter of hours, depending on the program of measurements ( a minimum of two additional Maxwell-rail-gap switches is required to meet the optimization conditions of the W > 100 kJ-PF).

In order to decrease the chamber contamination, a completely oil-free vacuum system is connected with the W > 20 kJ unit  The vacuum system includes a turbo-pump with a matching oil-free rough pump, both of Varian. The same institution that provided switching and triggering system did provide, under equal conditions during the completed project, also the vacuum system

The specifications of this upgraded unit, from which the main part of the data reported in Chapter 3 were obtained, are described in Appendix I.

Fig. 1

(a): New W $\geq$ 20 kJ PF machine.
The compact turbo pump
system is at the bottom
center.
The Ag-activation counter
is at the top left, a
scintillation detector at
the top right.



PF with
W $\geq$ 20 kJ
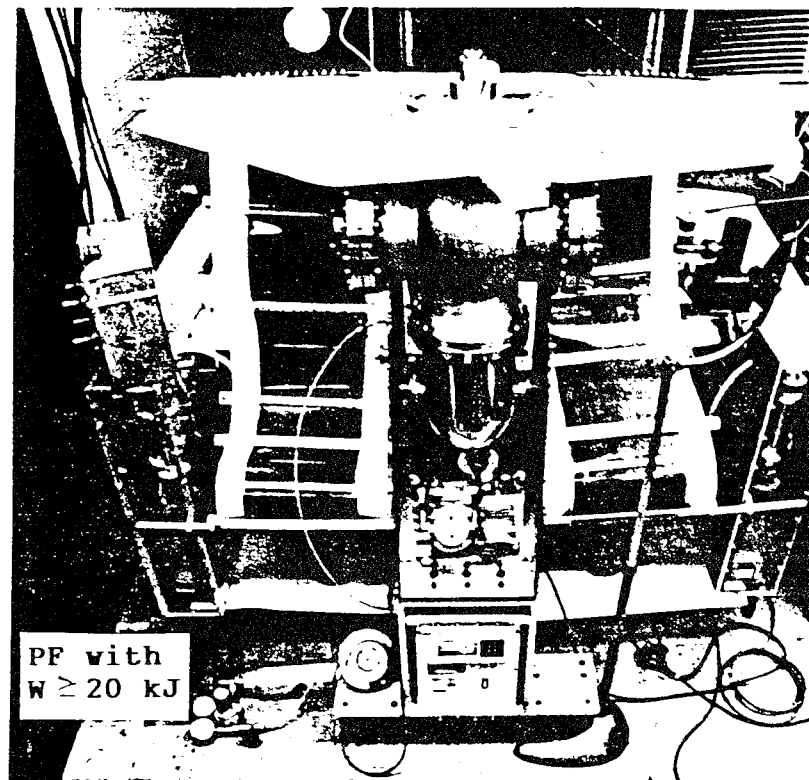
(b): Assembled W $\geq$ 100 kJ PF
system in the SIT Griffith
Bldg., with two level racks,
20 capacitors at each level.
Double-shielded cables with
solid copper shielding (top side)
transfer the electrode current
signal to the screened data-
acquisition room.



PF with
W $\geq$ 100 kJ
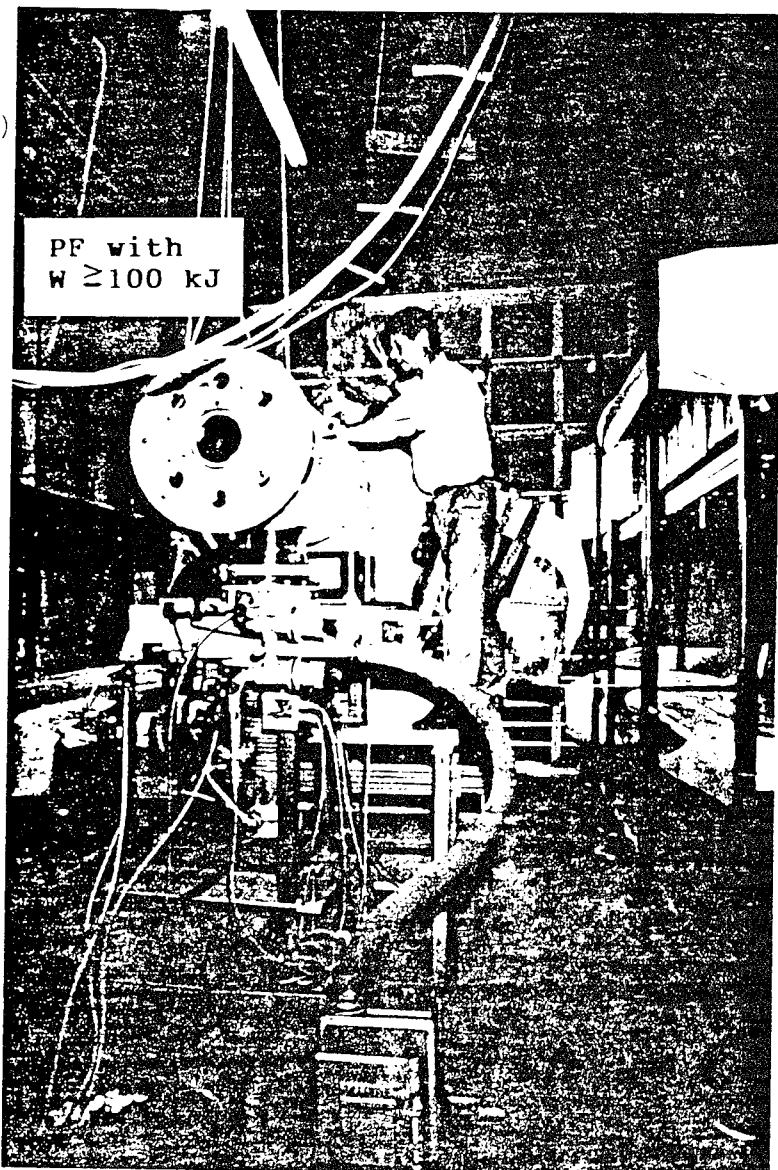
## 2. Scaling Laws For Plasma Reactivity and For Ion and Ion Cluster Emission

The neutron-yield scaling $Y \simeq K\,W^n$, with $n \simeq 2$ and $K$ = constant (not dependent on $W$ ) is a well established result, on a worldwide scale since many years, for optimized PF machines with Mather's geometry electrodes. One of our objectives under the AFOSR project was the verification of this scaling also for PF machines with an FDE-enhanced yield $Y$.

This was accomplished in the interval $5\text{ kJ} \le W \le 30\text{ kJ}$ with entirely positive results. The FDE-increased neutron yield $Y$ also increases for increasing value of $W$ as $W^2$. The ratio $Y$(with FDE) / $Y$(without FDE) $\ge 3$ is independent of $W$ in the tested interval. This type of tests involved three PF machines, with $W = 5$ kJ, $W \simeq 7$ kJ and $W \ge 15$ kJ [the latter by a mode of operation of the new $W > 20$ kJ PF system].

A second objective was the measurement of the ion and ion cluster fluence in different directions by using CR-39 targets. Differential filters were used to map the ion population in selected intervals of the ion energy spectrum. The etched ion tracks on the filtered target provide a detailed account of the ion distribution. Three independent methos were used:

(a) Pinhole imaging of the source (the PF pinch) and simultaneous filtering with a thin yarn mesh. Each nylon yarn of the mesh resting on the target surface had a 50 μm diameter and performed as a high-space resolution filter (space resolution of about 50 μm). The image space resolution is determined by the pinhole diameter (either 75 μm or 150 μm). An X-ray film behind theCR-39 target records simultaneously the X-ray pinhole image of the source. This sandwich detector of ions and X-rays is one of our diagnostic methods extensively used and reported in the literature [2].

(b) Target exposure to a single discharge without pinhole. The Cr-39 target with filter is fully exposed to the impacting plasma. This procedure provides a *contact print* of the impacting plasma via the nonuniform distribution of etched ion tracks, as in the case of the pinhole image. The ion track contribution of the impacting plasma to the image far exceeds the contribution from the pinch emission. This type of image provides a detailed structure of the impacting plasma, with a resolution determined by the thickness $\delta$ of the ion filter (see next Chapter 3).

(c) Compact Thomson (parabola) spectrometers with CR-39 targets. The high frequency electric field applied to the spectrometer magnet poles provides a ~1 ns time resolution. This method is described in reference [1]. In this project we have coupled a compact spectrometer with a pinch-image forming target by attaching a CR-39 plate to the front side of the spectrometer. A 250 μm diametr pinhole in the thin plate ( thickness 200 μm ) overlaps the entrance pinhole of smaller diameter (~193 μm) of the compact spectrometer. The first pinhole for the differential pumping, between the discharge chamber and the spectrometer chamber, performs also as pinhole-camera imaging system (this pinhole has a diameter of 190 μm; see Fig. 2).

During this project we have used also a time resolved (via time-of-flight) method for determining the time resolved ion spectrum. In this method the ions are collected by a carbon Faraday-cup, located after the pinhole for beam estraction and differential pumping. The results of these measurements coincide, within the experimental error, with

the results of time integrated method of much higher resolution (dE/E ~ 0.5% , in the interval 1 MeV < E < 6 MeV) as we reported in the publication No. 3 listed in Chapter 5

A third objective was a verification of the reaction yield of D + high-Z nuclei (Z > 1) as $^3$He, $^{12}$C, $^{14}$N, with a substantially-higher energy threshold than that of D + D and D + T reactions. This was accomplished with an array of 15 Geiger counters inside the discharge chamber, to monitor the $\beta^+$ decay of the nuclei generated in the reacting plasma and in solid targets of different materials. These reactions determinine the ion energy distribution in localized regions of high reactivity in the plasma from a comparison of the yield of different reactions (with different values of the energy threshold) in the same PF discharge [publications No. 1 and 5].

The different response of each Geiger at a different azimuthal position determine the azimuthal (nonuniform) distribution of the high-Z fusion reactions. Suitable numerical methods were developed to unfold also the radial position of the regions of high reactivity. These numerical methods utilize the data simultaneously obtained from the 15-Geiger-counter array in the same discharge. Detailed information on this procedure is reported in the publication No. 5 listed in Chapter 5 of this report, and in the 1992 and 1994 reports submitted by Stevens Tech to the AFOSR under the same contract AFOSR-91-0158. [We further refer to these reports as SIT-Rep-92 and SIT-Rep-93.] Different gas mixtures were also used, with a different fractional composition of the same gases in the mixture, in different series of tests. The variations of the fractional composition spanned a wide interval from ~ 5% to 50% by pressure.

A fourth objective was to determine the ion space distribution at high energy values ( ion energy E > 300 keV ) with different, mutually independent methods. These included ion track etching on filtered targets and measurement of the plasma reactivity and of its space distribution. within fragments of the PF current sheet ejected away from the axial pinch region.

The CR-38 targets with mylar filters were located at a distance 25 cm < L < 150 cm along the electrode ( z ) axis, and other targets at a radial distance $R_o$ = 11.4 cm from the axis. Suitable shields. an example of which is reported in Fig. 2, were used to protect the targets during the conditioning discharges. Both metallic and non-metallic target supports were used for the 0$^o$ targets (non metallic supports were always used for L > 50 cm).

A variety of other diagnostic methods reported in the literature, were used in parallel with new methods. as that reported in the next Chapter 3. These standardized methods include scintillation detectors of X-rays and neutrons (time resolution ~ 3 ns), Ag-activation silver counters of neutrons (Los Alamos design), magnetic probe measurements of the current-sheet propagation speed and structure, schlieren and shadowgraphy.

One of the new results was the observation of the *stuttering mode* of propagation of the current sheet, during the roll-off stage from the interelectrode gap and during the radial compression till pinch formation [publication No.4]. The observation was made with long-exposure schlieren imaging of the current sheet, by using a 0.1 GW ruby laser source, with pulse duration from 10 ns to ~ 50 ns. This stuttering propagation is unambiguously reflecting the oscillating processes in the interelectrode gap and in the

plasma during the energy transfer to the pinch region, with oscillation period of ~ 15 ns or longer.

### 3. Plasma Structure Imaging Via Nonuniform Distribution of Etched Ion Tracks on CR-39 Targets. Basic Concepts and Data Interpretation

Two PF machines optimized for the D + D neutron production, one at the energy level W = 5 kJ (17 kV), the other at W = 15 kJ (25 kV), were utilized for the target exposure. All CR-39 targets were exposed to a single discharge. The objective was to determine the scaling laws relating the discharge powering energy W with the total energy E ( ion kinetic energy and field energy of total density $\varepsilon = \varepsilon_k + \varepsilon_f$ in a plasma volume $\varpi$ ) of the self-field-dominated plasma lumps ejected from the pinch region. Three targets ( in the $0°$, $90°$ and $270°$ directions, respectively) were simultaneously exposed to a single discharge (see Fig. 3).

Five conditioning discharges were carried out immediately after each new set of three targets was loaded into the discharge chamber, without exposing the targets. The conditioning discharges offset the detrimental effects to the quality of the pinch which are introduced when the electrodes and the inner wall of the discharge chamber are exposed to oxygen in the ambient air, during the target loading operation. The quality of the pinch is defined in terms of the magnitude of the neutron yield. After the conditioning discharges the neutron yield per discharge Y rises again to values close to its mean value, $Y_{av}$, as determined from hundreds of discharges. The substantial decrease of Y after PF-components are exposed to air is a well known effect. No further discussion of physical processes related to PF contamination is included here.

Three mobile metallic shields protected the three targets from the plasma lumps ejected from the pinch during the conditioning discharges. The fixed targets are exposed by pivoting semicircular shields $180°$ about their support point at the center of their straight side. After exposure to a single discharge, the three targets were removed and etched for three hours in a 6.25 N solution of NaOH at 70 °C. The entire target surface was fully exposed to the pinch plasma source. The nonuniform distribution of etched D$^+$-ion tracks on the CR-39 target records the **contact-print** of all plasma lumps impinging on the target in a single discharge. The targets are covered with a mylar foil in tight contact (unless otherwise indicated) with the CR-39 target surface. The foil of thickness $\delta$ screens out all ions of energy, $E_d$, smaller than the chosen value, $E_{d.min}$ ($\delta$). We use $\delta$ = 25 μm to filter out ions with $E_d \leq 1.5$ MeV and $\delta$ = 50 μm to filter out ions with $E_d \leq 2.3$ MeV reaching the target. Clear contact-prints of plasma lumps with sharply defined boundaries (see Fig. 3, 4) were observed (see Fig. 3, 4) on more than 50 % of all exposed targets. The $90°$ and $270°$ targets of dimensions 5 cm x 7.5 cm ( facing each other, at opposite sides of, and parallel to, the electrode axis, z ) were at a radial distance R = 11.4 cm from z. The $0°$ targets were located at an axial position L (L had different values in

different discharges, 29 cm or 38 cm, with the z axis orthogonal to the target surface at its center ). The boundary sharpness of the contact-prints is characterized by a factor 10 drop in ion tracks/cm$^2$ on the CR-39 target surface over a distance of ~10 – 20 μm. The contact-print image of a plasma lump, at 0°, at 90° or at 270° frequently has a typical filamentary structure with filament widths of ≥ 100 μm. The linear dimensions of an entire image may exceed 1 - 3 cm.

Different models can be considered to connect the ion acceleration during the plasma impact on the filtered target to the plasma self-field decay . (i) The MeV ion emission occurs from extended plasma domains via nearly monoenergetic ion streams or, alternatively, via streams with a broad energy distribution. We have extensively verified both types of events in the explosive disintegration of the plasma structure with isotropic ion acceleration and emission. (ii) The ions are predominantly accelerated in the direction orthogonal to the filter surface. This is the case if MeV voltage pulses are established between the target grounded support [on the target back side] and the impacting plasma structure on the screened target front side. On the other hand, all our targets with floating dielectric supports also exhibit the same fine (filamentary) plasma structure as do targets with grounded metallic supports. These data justify our discarting (ii) and choosing (i).

If ρ is the ion range inside the filter, its dependence, $\rho = \delta/\cos\theta$; on the ion incidence angle θ ( the angle between the undeflected ion trajectory and the direction orthogonal to the target surface ) is smooth enough to generate a diffuse boundary of any plasma structure image, unless the ion energy spectrum meets strong constraints. If the ion emission from the plasma structure is isotropic over a broad energy band, or it is not confined to a very narrow energy interval, then the image should have a diffuse boundary and no sharp elements Quantitatively, the sharpness of the plasma image is described by the width $d_o = 20$ μm $= \delta \times \tan\theta$ of the target area over which the track density typical of a filament image drops by at least a factor 10 (we frequently observe also lower values $d_o$ ≤ 10 μm). If $\delta = \delta_1 = 25$ μm, the range increase $d\rho_1 = \delta_1/\cos\theta - \delta_1$ along the direction $\theta_1 = \tan^{-1}d_o/\delta_1 = 0.68$ radians, such that $\cos\theta_1 = \delta_1/\rho \sim 0.78$, is $d\rho_1 \sim 7$ μm.

For $\delta = \delta_2 = 50$ μm, $\theta_2 = \tan^{-1}d_o/\delta_2 = 0.38$ radians, $\delta_2/\rho = 0.93$ and $d\rho_2 \sim 4$ μm. The stopping power increase corresponding to dρ screens out ions with energy $E_d \leq 1.8$ MeV with an increase of $E_{d,min}(\rho)$ of about 20% for the 25 μm filter, and of about 5% ( from ~ 2.3 MeV to ~ 2.4 MeV ) for the 50 μm filter.

This relatively weak increase of the filter stopping power with θ sets a limit of ~5% for the energy spectrum width of the accelerated ion streams in order to explain the image sharpness in terms of dρ(θ). A concentration of the accelerated ions in a spectrum interval of width $dE_d$ such that $dE_d/E_d \simeq 5\%$ fits our observation of sharply defined boundaries of the plasma filament images with $E_d > 1.5$ MeV and $E_d > 2.3$ MeV ion tracks. A concentration of the ion population in narrow intervals of the energy spectrum

is frequently observed via Thomson (parabola) spectrometer data of all our PF machines from W = 5 kJ to W $\geq$ 15 kJ (see next Chapter 4) and is typical of the ion emission from the disintegration of ion clusters and superclusters.

Other data (Fig. 4), were obtained by inserting a variable spacing $\Delta$ < 1 - 2 mm between ion filter and CR-39 target. These data indicate that the ion isotropic emission from the impacting plasma structure is not easily reconciled with the observed disappearance of the track-formed-image over portions of the target area, where $\Delta \sim$ 1 mm. The difficulty of interpreting these data is not entirely eliminated even if we consider the ion confinement within a very narrow interval of the energy spectrum. In the case of isotropic ion emission, an increase of $\Delta$ induces the image blurring from the loss of space resolution, i.e., of image details of linear dimensions 10 - 20 $\mu$m, but does not imply the disappearance of the blurred image. The $\theta$ dependence of the filter stopping power is not affected by $\Delta$. $\Delta$ bears only on the image space resolution but not on the mean value of the ion track per unit surface, if (a) the ion source is not localized within a small volume but covers a wide area on the front side of the mylar filter, and if (b) the ion trajectories after the filter crossing are straight lines. We have verified (a) on many CR=39 targets with a vanishing image of the impacting plasma where $\Delta$ > 0.

Consistently, we must address (b) in order to explain the critical role of $\Delta$ in the image formation process.

Fig. 4 shows that over a wide area of the screened target (T-B-17) the spacing (target area of low ion track density) between sharp components of the plasma structure image (with a high ion track density) can be smaller than the width of these image components of high track density. The total ion emission is expected to provide a wide-area image, of the same dimensions ( > 1 - 2 cm ) of the entire impacting plasma structure, because of the mutually-reinforcing ion contributions to the CR-39 image from neighboring regions of the impacting plasma.

This is not what we observe if we move from a selected target area with sharp filamentary image to a neighboring area of the same target where $\Delta$ was increased to $\simeq$ 0.5 mm. The image fading ( for $\Delta \leq$ 0.5 mm ) and disappearance (for $\Delta$ > 0.5 mm), point to a mechanism of ion acceleration and to ion propagation which involve critically the spacing $\Delta$. This observation does not simply fit an ion beam propagation in the direction nearly orthogonal to the ion filter/target surface

The existence of a strong magnetic field B within the spacing $\Delta$ can explain the image disappearance by eliminating (b)  The magnetic field may leak through the mylar filter because of polarization current pulses in the mylar filter and, for a small $\Delta$, in the in the CR-39 target. The disruption of the electron current patterns and of the self-field structure in the plasma, during the plasma impact, creates polarization current pulses via the induction electric field pulses in the same direction of the plasma current. The electrons are the current carriers in the plasma. The resistivity surge at the impact time generates displacement current, polarization current in the dielectric material and dielectric surface current. In order to prevent the image formation on the CR-39 target the D-ion radius of curvature r [ r(cm) $\simeq$ 6.46 $E_d^{1/2}$(keV)/B(kG) ] in the leaking magnetic field B within $\Delta$ must be smaller than $\Delta$.

This condition is met if we assume the bulk of the image-forming population of ions to have a minimum residual energy $E_d(\rho) \simeq 10$ keV after crossing the mylar filter. The magnitude of the leaking magnetic field B can be easily assessed under the simplifying assumptions:

(i)      a fraction i/I of the total electrode current I flows in a plasma strip of width $\alpha$ of the impacting plasma.

(ii)      the induced current, $i_d$, in the impacted dielectric strip of nearly equal width $\alpha$ is of the same order of magnitude of i, i.e., $i_d/I \sim i/I = \eta$. We may use $\eta$ as a convenient parameter in terms of which to gauge the azimuthal anisotropy of the plasma current in the off axis region of a PF discharge.

The targets of Fig. 3, 4 were exposed (at a radial distance $R_o = 11.4$ cm from the electrode axis) in the 15-kJ-PF machine with peak electrode current $I_M \geq 0.8$ MA

The estimate $i = I_M \times \alpha/2\pi R_o$ corresponds to the assumption of an azimuthally uniform current distribution in the off-axis plasma, in the form of an uniform current sheet which expands radially to the distance $R_o$ in a time $t \leq 1$ µs ($< T/4 = 2.5$ µs). We define the azimuthal anisotropy factor $S_i$ for the off-axis plasma current as $S_i = (\eta - \eta_o)/\eta_o$ [$\eta_o \equiv \alpha/2\pi R_o$]. We adopt a similar definition of azimuthal anisotropy factor, $S_n$, for the image-forming plasma as for the current-carrying plasma. The plasma image at 90° and 270° is usually formed on a strip of width $\phi$ of target surface (stretching along the z-axis for the entire length $\lambda_o$ of the target) where the bulk of low-energy ion tracks of minimum density $\nu_o = 5 \times 10^6$ cm$^{-2}$ is concentrated. This minimum density $\nu_o$, or a higher density, of shallow tracks (of depth $\leq 1$ µm) is necessary to form the milky pattern of the plasma image. In the definition of $S_n$ we must replace $\eta$ with $\zeta$, essentially the observed typical width $\phi \simeq 1.0 \pm 0.3$ cm of a 90° (or 270°) image, multiplied by a suitable normalization factor. The total number of image-forming tracks, N, replaces the measured value $I_M$.

$N = \nu_o \lambda_o 2\pi R_o \times (\Sigma\phi/32w_o)$, where the summation is carried out over all 16 pairs of targets (T-A, T-B), each of width $w_o = 5$ cm, from the same discharge. In the definition of $S_n$, $\phi$ replaces $\alpha$, $n = N\phi/2\pi R_o$ replaces i and $\eta_o$ is replaced by $\zeta_o = \phi/2\pi R_o$.

The inspection of 32 targets with exposure at 90° and 270° (2 targets, T-A, T-B, from each discharge, with a third target, T-C, at 0°), some with a plasma image, gives a typical azimuthal anisotropy factor as high as $S_n \geq 10 \pm 3$. The statistical error on $\phi$ and on $S_n$ ($\pm 30\%$) is that of a fitting Poison distribution of image-forming events. The elongated image is usually observed only on one of the two targets T-A, T-B from the same discharge. In agreement with our data, we now take $S_i \simeq S_n$. The cogency of this equality is confirmed also by a general observation: the space location of the current-controlled ion-acceleration process must unambiguously and quantitatively correlate with the image formation area on the filtered target.

In this case,      $B(\text{Gauss}) \simeq 4 \times [i(A)/\alpha(mm)] \tan^{-1}(\alpha/2R)$      at a distance      $R \leq \alpha$ ($\alpha < \Delta \simeq 1$ mm) from the back surface of the mylar filter. If, for example,

$i \sim 10$ kA [S = 10] and $\alpha \sim 0.5$ mm [ from Fig. 4 ], then at any $R \leq \alpha$ we have:

$\tan^{-1}(\alpha/2R) \geq 0.46$ radians,

$B \geq 3.68 \times 10^4$ G and

$r[E_d(\rho)=10 \text{ keV}] < 0.56$ mm.

If $i \sim 12$ kA [ S = 12 ], then $r < 0.5$ mm.

Note that a fraction of the dielectric (polarization) current can be carried by the CR-39. The polarization current in the CR-39 increases by decreasing values of $\Delta$ and, consistently, B decreases within the spacing $\Delta$ for decreasing values of $\Delta$. The distribution of dielectric current in the mylar filter and in the CR-39, and so the strength of B in $\Delta$, are nonlinear functions of $\Delta$.

We conclude that the existence within $\Delta$ of a pulsed magnetic field $B \sim 10^4 - 10^5$ G provides an acceptable explanation of the critical dependence on $\Delta$ of the image formation process and of the plasma-image disappearance for $\Delta \geq 0.5$ mm. This conclusion provides also a method of determining the lower bound $\varepsilon_{min}$ of the initial energy density $\varepsilon$ in the impacting plasma.

## 4. Energy Density Within Self-Field-Dominated Plasma Sources of Ion and Ion-Cluster Beams. Conclusions.

The observed spectra reported in Fig. 5 from a Thomson parabola spectrometer provide an example of sharp spectral peak in the low-energy ion component of our 5 kJ-PF source. The spectra from the > 20 kJ system have essentially the same characteristics.

We estimate the ion kinetic energy $\varepsilon_{k,l}$ from the observed ion fluence $d^2\psi/dE_d d\theta$ at a distance $\delta = 50$ $\mu$m from the source for a narrow interval $dE_d \sim 10$ keV at $E_d = 2.3$ MeV. The spectrum is sharply peaked wthin $dE_d$, with amplitude higher by a factor $\gamma \sim 3$ than the smooth amplitude $d\psi/dE_d \sim AE^{-m}$, $m \simeq 3$, in neighboring regions of the observed [1] D$^-$ energy spectrum.

To estimate the contribution $\varepsilon_{k,o}$ from all other regions of the ion spectrum, outside the narrow interval $E_d = 2.3$ MeV, $E_d + dE_d$, we calculate A by taking $d\theta = 0.38$ radian, $dE_d \simeq 10$ keV, and $2[d^2\psi/dE_d d\theta]dE_d d\theta = \delta^2 \times (10^7 \text{ cm}^{-2})/\gamma$ from the ion track count $v \simeq 10^7$ cm$^{-2}$ on the filtered CR-39 target image with peak $v$.

This estimate gives $A \simeq 4 \times 10^3$ (if $E_d$ is expressed in MeV).

Under the assumption of a spatially isotropic ion emission from a minimum plasma volume $\varpi \simeq (d_o)^3 = 10^{-9}$ cm (as defined from $d\theta$) on the front surface of the mylar filter, we have:

$\varepsilon_{k,l} = (4\pi/\varpi \, d\theta \,) E_d \, \delta^2 \, v \simeq 3$ J/cm$^3$,

$\varepsilon_{k,o} = \int E_d \, (d\psi/dE_d) \, dE_d \times \varpi^{-1} \simeq 300$ J/cm$^3$,

$\varepsilon_f = B^2/4\pi \sim 100$ J/cm$^3$,

$\varepsilon_{min} = \varepsilon_{k,l} + \varepsilon_{k,o} + \varepsilon_f \simeq 0.4$ kJ cm$^{-3}$.

The estimated density 0.4 kJ/cm$^3$ represents a lower bound of $\varepsilon$ and does not exclude substantially-higher values of the energy density in the ejected fragments of the PF current sheet. Contributions which can substantially increase $\varepsilon$ may come from:

(i)     An underestimate of the low energy ions (the integration over the energy spectrum to estimate $\varepsilon_{k,o}$ is carried out only above $E_d \geq 1$ keV; we also note that in several spectra $m > 3$ for $E_d < 0.5$ MeV).

(ii)     Electron energy, or at least some (thermal) component of it.

(iii)     Higher values of the magnetic field ($B > 10^8$ G fields form in localized regions, with linear dimensions of the order of 10 $\mu$m to 100 $\mu$m, of the pinch [2]).

(iv)     Energy dissipation effects during the small, but not negligible, time duration of the plasma impact and plasma-structure disintegration. These effects are not fully accounted for by the data from the time-integrated diagnostics reported in Chapter 3.

The scaling as a function of W, of the total energy stored in the ejected fragments of the current sheet, and of the energy of the ion and ion cluster emission is the same, within experimental errors, as the scaling $Y \sim W^2$ of the neutron yield/pulse, Y, from D + D fusion reactions. In agreement with all our laboratory tests, this conclusion applies also to high-Z fusion reactions as D + $^3$He, D + $^{12}$C, D + $^{14}$N in deuterium plasmas with fractions from 5% to 50% of high-Z nuclei in the filling gas. Since the threshold energy of these reactions is substantially higher than that of the D + D reactions we conclude that peak energy density in the plasma is the same for 5 kJ-optimized PF machines as for > 20 kJ-PF optimized machines. The general increase with W of a variety of emission components fits an increase of the source plasma volume with the same high energy density, rather than an increase of the peak energy density as a function of W.

We consider of great interest the sharp peaks of the ion spetrum as reported in Fig. 5 and the similar sharp peaks we observe in the W > 20 kJ PF machine. As an example, four peaks were observed, respectively at 150, 200, 300, 550 keV on a Thomson spectrometer target exposed to 32 discharges at 25 kV in 5 Torr of pure deuterium at this higher energy level.

These peaks are more frequently observed in the 80° than in the 0° spectra. Our explanation is that the ion cluster fluence across the high intensity magnetic field is substantially higher than the single-ion fluence across the same field. The cluster disintegration, in flight across the background plasma and/or on impacting the first pinhole edges, is then the source of the spectrum peaks. In this case the peaks would correspond essentially to the translation velocity of the clusters. If we assume that each spectrum peak corresponds to the random process of disintegration of a single supercluster with nearly isotropic emission in the center-of-mass reference system, we can aslo estimate its mass from the track count on the target at the entrance of the Thomson spectrometer and the distance between first pinhole and target. The result from this procedure fits the earlier findings from target damage assessment, on targets fully exposed to the impacting particle beam, without pinhole.
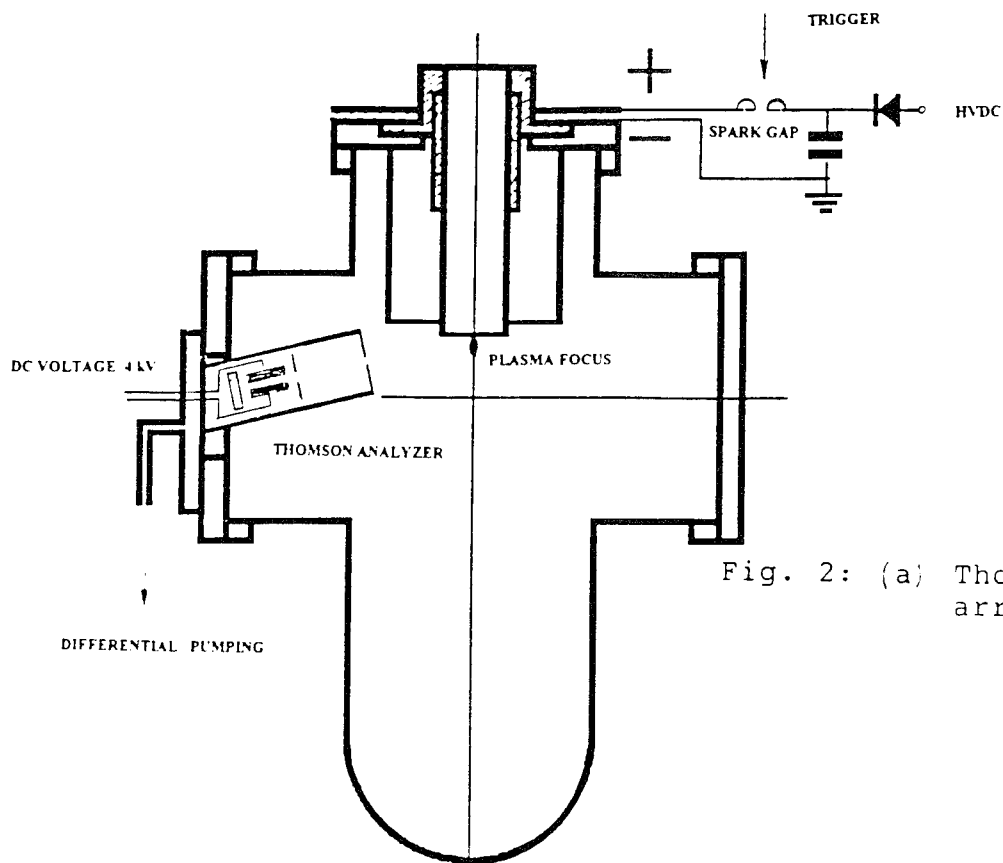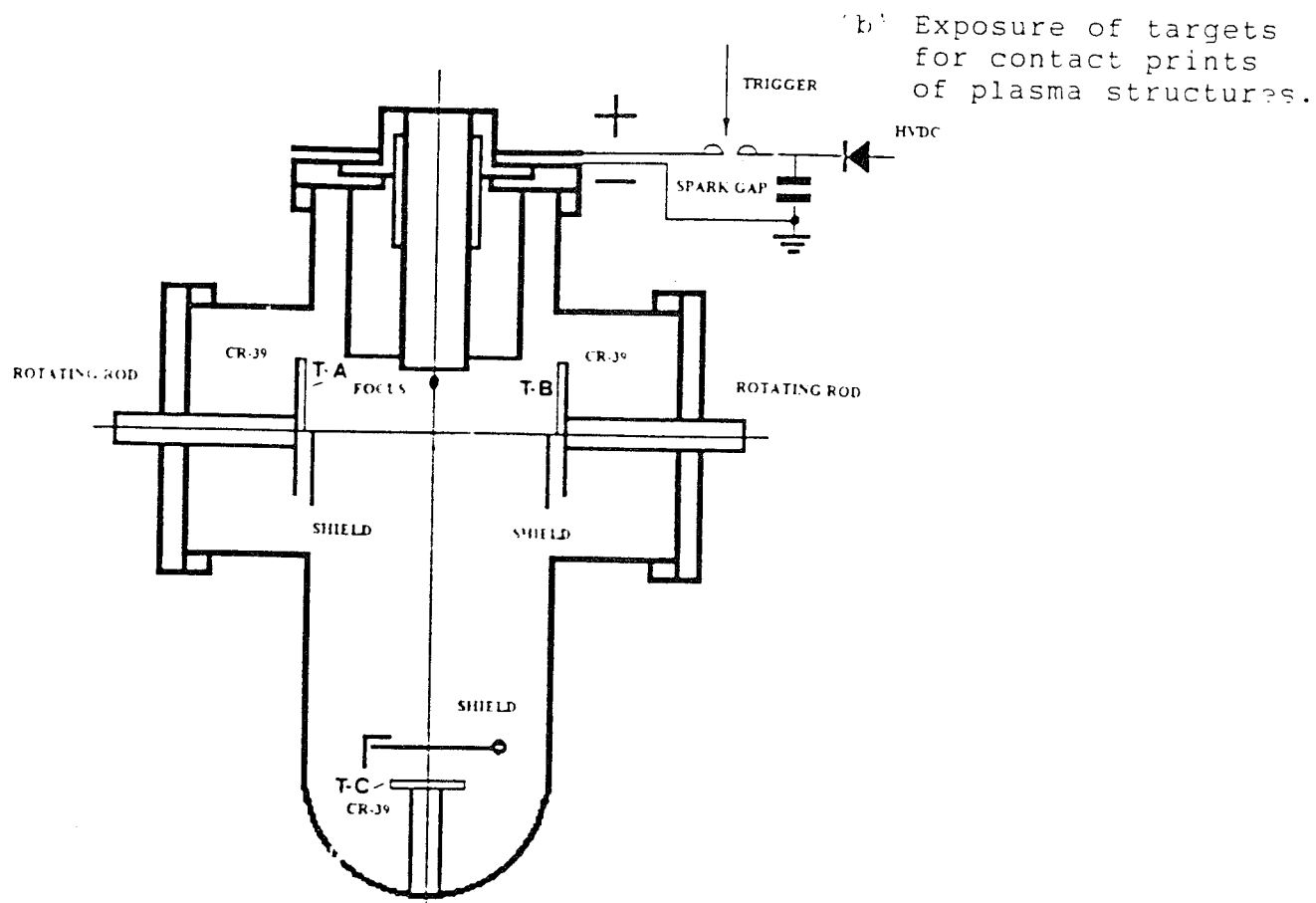
Fig. 2: (a) Thomson spectrometer
arrangement at 80°.

(b) Exposure of targets
for contact prints
of plasma structures.

Discharge chamber with electrodes of the W > 20 kJ PF machine. The center electrode
(anode) has a diameter of 5 cm.

## 5. Publications

1     High Yield of $^{12}C(d,n)^{13}N$ and $^{14}N(d,n)^{15}O$ reactions
in the Plasma Focus Pinch

J.S. Brzosko, V. Nardi, Physics Letters A, (1991),
Vol. 155, p. 162-168.

2     Fusion Reaction Yield in Focused Discharges with Variable
Energy and Plasma Fine Structure

J.S. Brzosko, H. Kilic, V. Nardi, C. Powell, J. Wang.
Proc. of 1992 Europ. Conf. on Plasma Physics and Nuclear
Fusion Research, Innsbruck, (1992), Vol. 1, p. 695-698.

3     Time Resolved Energy Spectrum of the Axial Ion Beam
Generated in Plasma Focus Discharges

W.H. Bostick, H. Kilic, V. Nardi, C.W. Powell.
Nuclear Fusion, Vol. 33, No. 3 (1993), p. 413-420.

4     Long Exposure Time Schlieren Photography of Plasma Focus
Discharges

K. Melzacki, V. Nardi: Review of Scientific Instruments,
(1994). Accepted for Publication.

5     Observation of Plasma Domains with Fast Ions and Enhanced
Fusion in Plasma-Focus Discharges

J.S. Brzosko, V. Nardi, J.R. Brzosko, D. Goldstein.
Physics Letters A, (1994). Accepted for Publication.

---

\* Four other papers are submitted for publication.
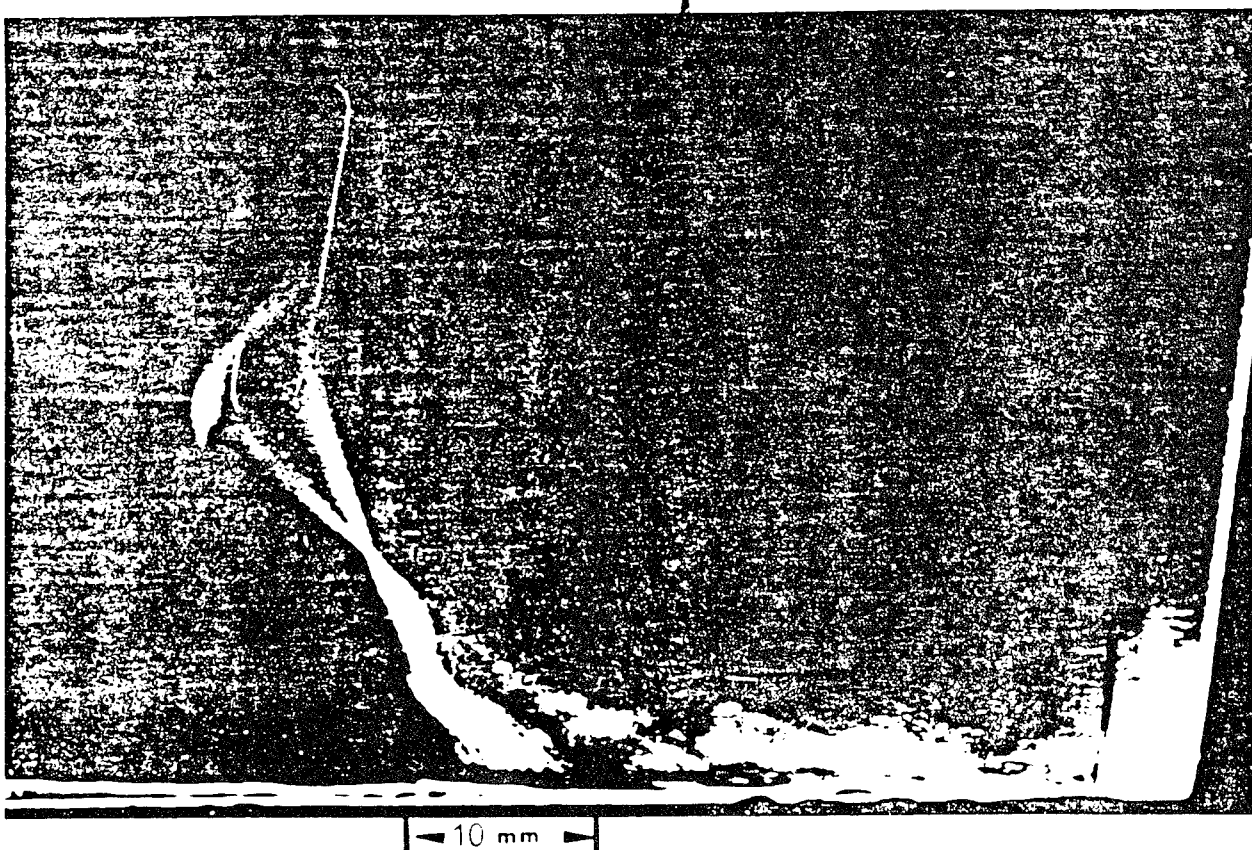
Fig. 3 (a)   Contact-print image of a laser-created plasmoid impacting on a
screened CR-39 target [1]. The image is formed by the non-uniform
distribution of [illegible] with energy E > 2.5 MeV in (A)
          in (B) ([illegible]). Note hot spots. The electrode axis
intercepts the center of (A), and (B) at lower right.

Upper photograph: Filamentary pattern of plasmoid (a forwardly
ejected fragment of the PF current sheath) from
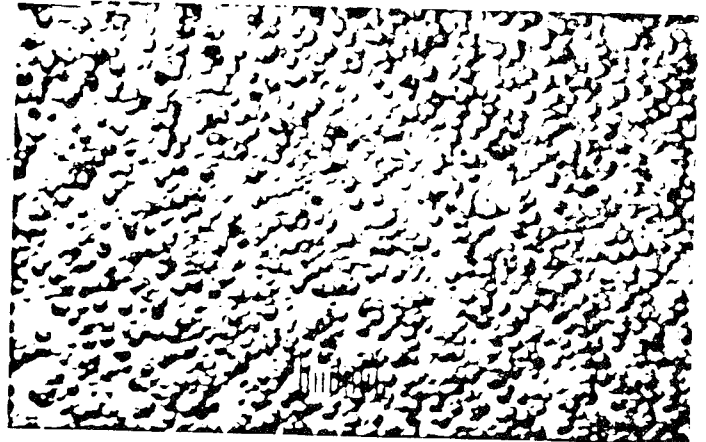the nonuniform distribution of $\geq 2.5$ MeV D$^+$-ion tracks
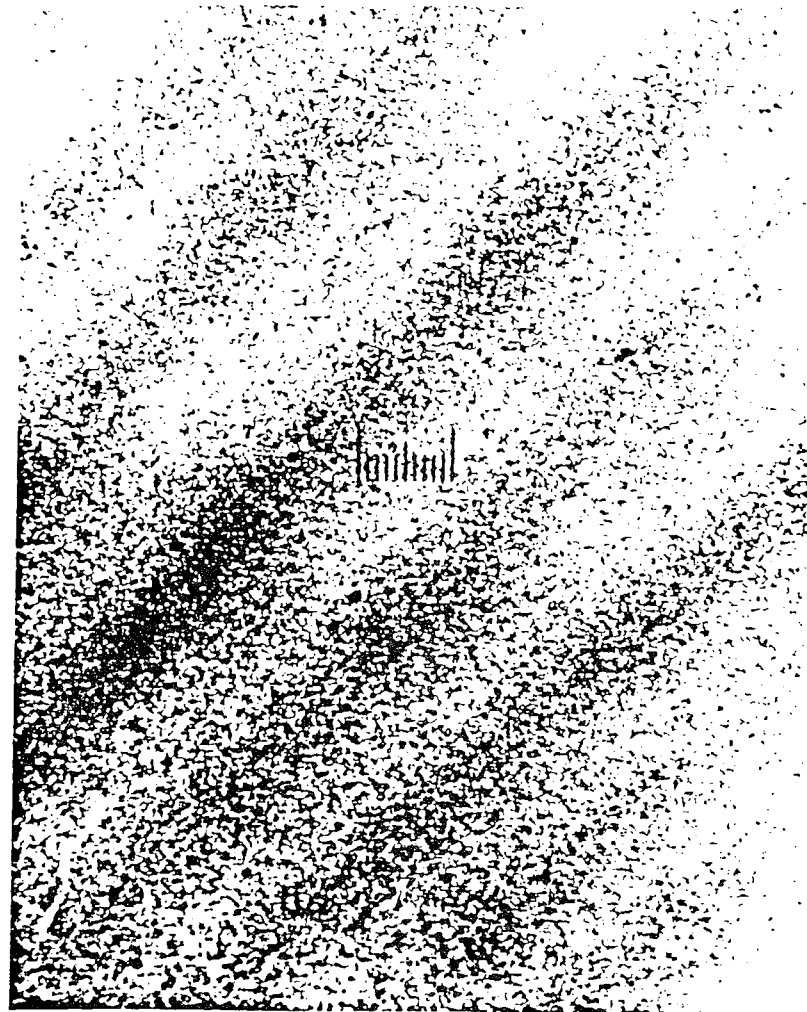
L = 25   cm

200 micron

>|          |<



10 micron

10 micron

Lower photographs: Ion tracks ( $> 2.5$ MeV D$^+$ ) on CR-39 target in the
location of the graticule between filaments (left)
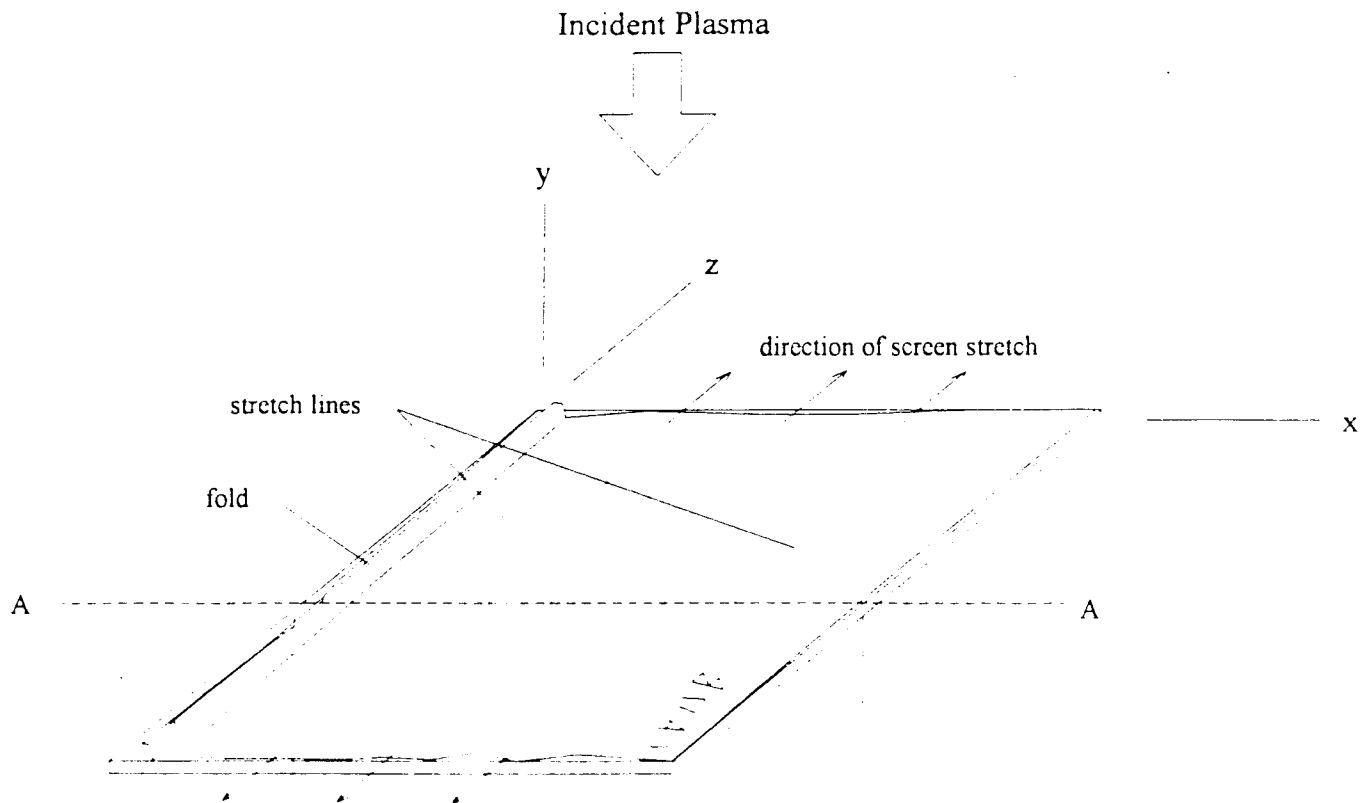and on the filament (right).

Fig. 3 (c)    Optical microscope photography of the fine (filamentary) structure of
the plasmoid contact print of Fig. 2a.  Details from the region as
indicated by arrow.  The track count is $7.1 \pm 1.0 \times 10^5$ on the
filaments $3.5 \pm 0.5 \times 10^5$ in the region between filaments (D$^+$-ion
energy $> 2.5$ MeV; the mylar filter covering the CR-39 target was 50 $\mu$m
thick).  The track count drops by a factor 2 over a distance of less
than 10 $\mu$m at the sharply defined edge of the filament.

Fig. 4        (a): Schematic view of the filter configuration to generate the image of Fig. 4 (c) at 90°. The ripples of the mylar filter were generated by stretching the filter along the z axis (orthogonal to the filamentary structure of the image). The relatively weak variations of the image intensity in the direction of the filametary structure correspond to a spacing < 0.5 mm between mylar filter and CR-39 plate during the exposure.. Note complete dissappearence of the image in (c), along the line of maximum distance (> 1 mm) between screen and target. This location corresponds to the b-location in (a). No stretching of the filter was imposed for the 0° eposure (Fig. 4-b image). Exposure to a single discharge of the W > 20 kJ machine (Fig. 1 a). All images are formed by the nonuniform distribution of ion tracks.
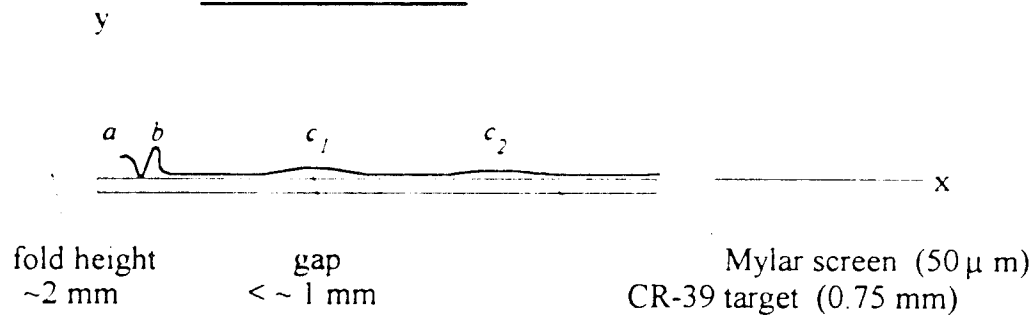
# CR-39 Target / Mylar Filter Configuration
## Deuteron Energy, E > 2.3 MeV

Fig. 4 (a)

Incident Plasma

y

z

direction of screen stretch

stretch lines

fold

A — — — — — — — — — — — — — — — A

x

## Cross-section A-A:

y

$a$  $b$      $c_1$          $c_2$

x

| fold height | gap | Mylar screen (50 μ m) |
|---|---|---|
| ~2 mm | < ~ 1 mm | CR-39 target (0.75 mm) |

*$a$, $b$, $c_{1,2}$ : points of no-contact between screen and target*

Conta   print image of impacting p   sma on CR-39 target
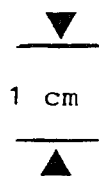recorded via Non uniform distribution of etched ion tracks

Target # CA-17-C

   mylar filter
   thickness

   $\delta = 50 \, \mu m$
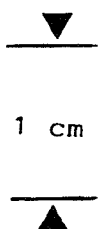
   Deuteron energy
   2.3 MeV

   $Y = 0.6 \times \bar{Y}$

▼
___
1 cm
___
▲

   $0^\circ$ direction

   L = 38 cm

Fig. 4

▼
___
1 cm
___
▲

Target # CA-17-B
  $90^\circ$ direction

d = 11.5 cm

V = 25 kV

5 Torr $D_2$

**a** ———Deuterium

$0^0$

$10^{13}$

$10^{12}$

Hydrogen ———

$d^2 \psi/dE\, d\omega$

$\sim E^{-7.0}$

$\sim E^{-7.5}$

$10^{11}$

T - 187

$0^0$ direction
single discharge in 50 % $H_2$ + 50 % $D_2$ by pres.
V = 17.5 kV
p = 3.7 Torr
Thomson spectrometer voltage 4 kV (B = 5 kG)
Single discharge exposure

E (MeV)

0.01          0.10          1.00

**b**          220 keV

$80^0$

$10^{12}$

$10^{11}$

33 keV

$d^2 \psi/dE\, d\omega$

$10^{10}$

T-117

$80^0$ direction
100% D2
p = 2.4 Torr
exposure to 12 discharges
other conditions are the same as in (a)

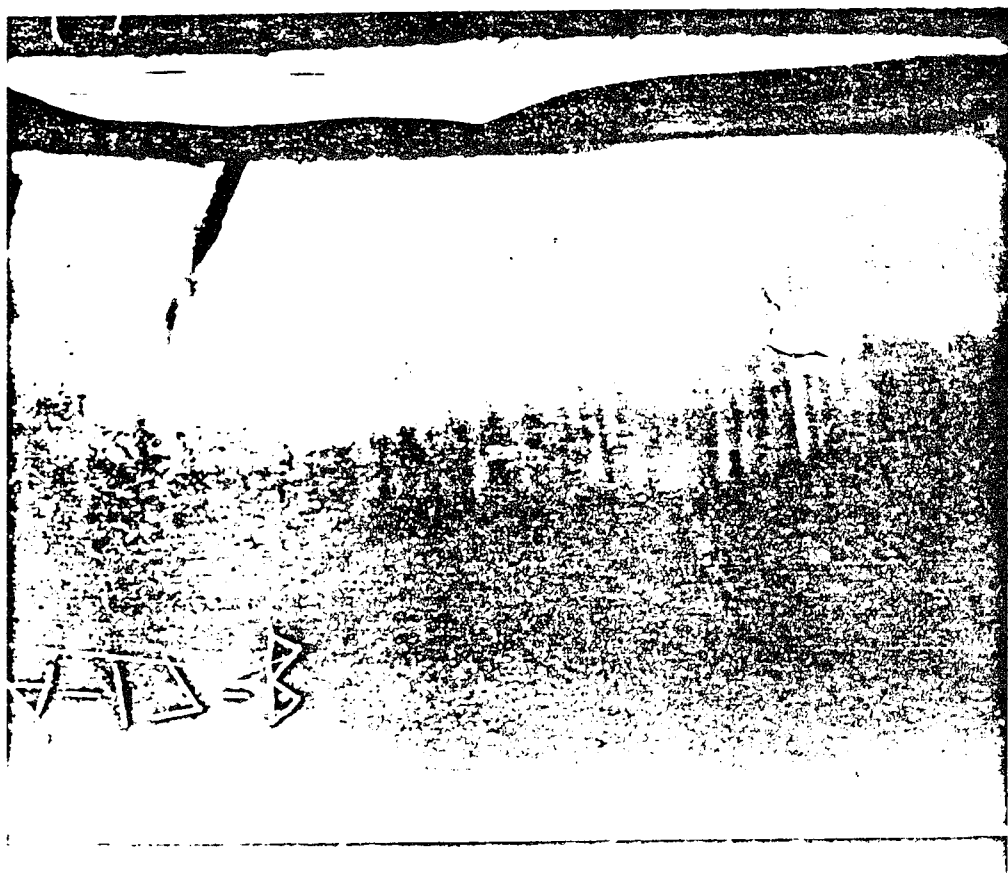E (MeV)

0.01          0.10          1.00
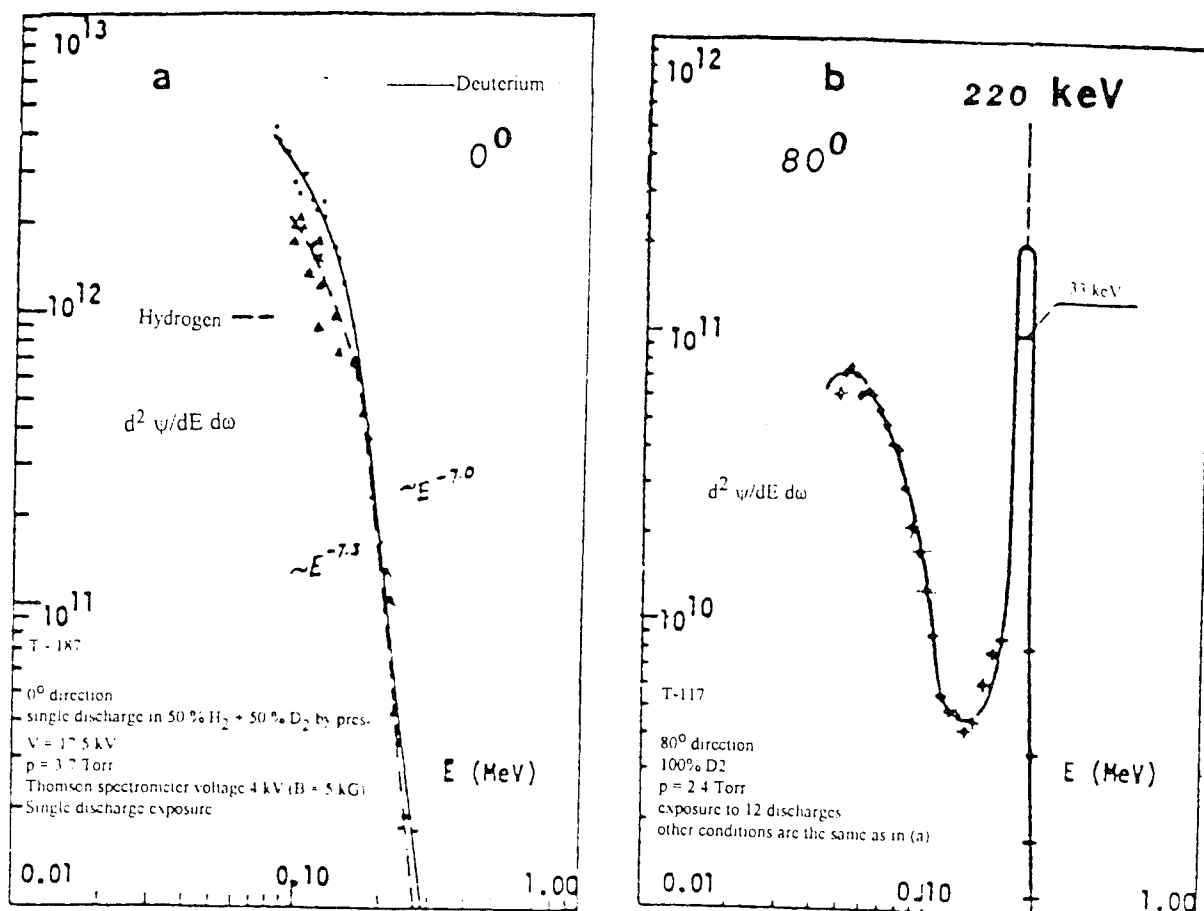
Fig. 5:      Thomson spectrometer data, for W = 5 kJ.
   (a) Note the typical sharp drop ($E^{-7}$) of the
       spectrum amplitude at $0^c$ between 200 keV and
       300 keV from a single discharge in a gas
       mixture of $H_2$ + $D_2$.
       The decreasing of the spectrum amplitude above
       0.5 MeV is weaker, $\sim E^{-3}$ .

   (b) Pure deuterium spectrum in the $80^c$ direction with
       a narrow energy band of width dE = 30 keV at
       $\cdot$ E = 220 keV. The spectrum is obtained from
       12 discharges. Sharp spectral peaks are typical
       of the ion cluster disintegration on impacting
       the first pinhole, i.e., the aperture of the
       differential pumping system close to the source
       is at a distance of 95 mm from the electrode
       axis. The distance between first pinhole and
       second pinhole, at the entrance of the Thomson
       spectrometer, is 41 mm.

       Similar sharp peaks are also present in the ion
       spectra at $80^0$ of the $W > 20$ kJ PF machine.
       The spectrum in (b) was obtained from the ion
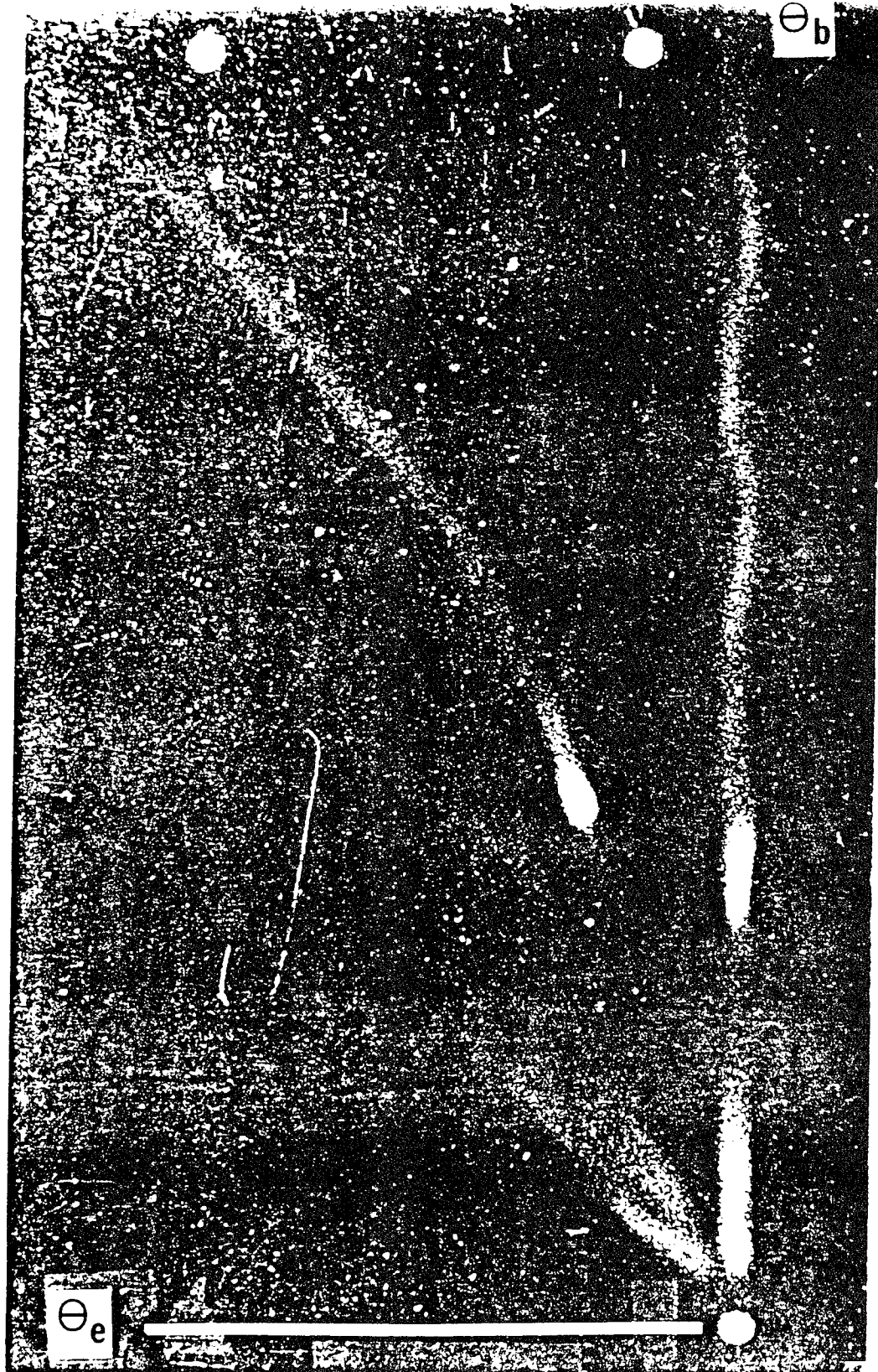       track parabola of Fig. 5 (c).

Fig. 5   c

# Appendix I : Coaxial Gun Specifications

The imploding current sheet is generated by a plasma focus machine (PF) with Mather's geometry of the electrodes. The quality of the pinch and of the radially-converging plasma sheet, with a maximum current density between the electrodes, is conveniently assessed from magnetic probe data and also via the neutron yield per pulse from D + D reactions. As a rule, in a series of test discharges in pure deuterium or in a mixture containing deuterium, the highest neutron yield is measured when the interelectrode current has a *sharply-peaked* distribution rather than a *diffused* space distribution. Neutron yield measurements for a pure-deuterium-filled discharge chamber (Fig. 1    Section 2) are reported in Table I from each of two series of > 50 discharges at a relatively-low voltage. Under the chosen conditions, the occurrence of a multiplicity of current sheets and of related complications is minimized. Detailed information on the current distribution in the sheet and the sheet velocity v are obtained by magnetic probe measurements, as reported in Fig. 1 of this Appendix. The first of two probes, ( P-1 ), is always located just above the edge of the hollow center electrode(anode), i.e., at a radial distance from the electrode axis equal to the anode outer radius $r_o$= 26 mm. The second probe, ( P-2 ), is at a radial distance of 1 cm from ( P-1 ), *inside*, or in other tests *outside*, the anode edge, depending on the position at which we want to determine v(r, z). Both probes are on the same plane orthogonal to the electrode axis, at a distance $z_p$ = 1 cm above the edge of the anode. The outer electrode (cathode) has inner radius R=64 mm (38 mm interelectrode gap). The inductance of the powering capacitor bank of total capacitance C = 60 μF ( two modules, each with 5 Aerovox capacitors of 30 nH, 6 μF, 10.8 kJ at 60 kV) is 3 nH. One rail gap switch of inductance 20 nH is used for each modules (Maxwell model # 40200, max. current 750 kA, max. voltage 100 kV; jitter < 2 ns). The two switches are closed by a voltage pulse from a 100-kV-multiple-trigger generator (Maxwell mod. # 40151, 10 outlets, rise time < 1 ns, jitter < 10 ns), activated by a master 100-kV-trigger (Maxwell mod. # 40295 jitter < 7 ns; rise time < 0.2 ns).

**Table 1.** *Leading figures of merit (peak electrode current $I_M$, energy input W, neutron yield Y per pulse) of driver, a PF with max. W ≈ 100 kJ at 60 kV. Period 9.0+/-0.1 μs.*

| capacitor bank powering energy & peak electrode current | neutron yield per pulse maximum value | neutron yield per pulse mean value | $D_2$ filling pressure for maximum yield |
|---|---|---|---|
| W (kJ), $I_M$ (MA) | Max Y(D+D) | $\overline{Y}$(D+D) | p |
| 13 kJ, 0.8 MA (21 kV) | $0.5 \times 10^{10}$ | $1.2 \times 10^9$ | 5 Torr |
| 18 kJ, 1.0 MA (25 kV) | $1.6 \times 10^{10}$ | $1.6 \times 10^9$ | 6 Torr |

The inductance, up to the breech end of the electrodes, including power transmission plates, is $L_C$ = 14 nH. The inductance of the interelectrode gap, from breech to muzzle

side of the anode end is $L_e = (\mu_o/2\pi) \, l_o \ln(R/r_o) = 26$ nH (anode length $l_o = 145$ mm) The circuit total inductance under *static* conditions is $L_o = L_C + L_e = 40$ nH. From the *measured* period $T = 9.0 +/- 0.1 \, \mu s \simeq 2\pi \, ( \, LC \, )^{1/2}$ of the complete circuit (powering system and electrodes, with the moving plasma sheet in the interelectrode gap), the corresponding value of the total inductance under *dynamic* conditions is $L = 34 +/- 1$ nH. The dynamic inductance accounts for the resistivity $R \simeq dL/dt = v \, L_e/l_o > 23$ mOhm to 46 mOhm, where $v \geq 4 \times 10^6$ cm/s to $10^7$ cm/s is the measured current-sheet velocity after rolling off the interelectrode gap, till the beginning of the radial compression phase [ if $R > 0$, then $L \simeq (T/2\pi)^2 [ \, 1/2C + (1/4C^2 - \{2\pi/T\}^2 \, R^2/4 \, )^{1/2} ] < L_o$ ].

The two reversals in each of the P-1 signals in Fig. 1(a) and (b) indicate that three current sheets $CS_1$, $CS_2$, $CS_3$ are sweeping the magnetic probe in these discharges. The neutron yield depends on specific characteristics of the layered structure of the current distribution. Specifically, Y is strongly dependent on the time delay $\Delta t_2$ between the leading $CS_1$ and the trailing $CS_3$ and, to a lesser extent, on the delay $\Delta t_1$ between $CS_1$ and $CS_2$, in agreement with the equation $Y \simeq \bar{Y} \, x[ \, \alpha \, (\Delta t_1)^{-n} + \beta \, (\Delta t_2)^{-2} ]$, with $n > 2$, and $\alpha << \beta$ . $\bar{Y}(W,p)$ is the Y mean value from all discharges with the same W, p. The major number of discharges has a sufficiently-high value of $\Delta t_1$ (as those of Fig. 1), so that the first $\alpha$-term can be neglected. By expressing $\Delta t$ in nanosec we have $\beta(W,p) = 1.6 \times 10^5$ ns$^2$. Further insight on the equation relating Y and the $\Delta t$ ' s is gained from its derivation, similar to that of Hartline and Ratliff equations for neural networks [1]. In our case, the i-th *response* function is the i-th contribution to the neutron yield from the i-th imploding current sheet; the *input* intensity ($\simeq dI_i/dt$) is determined from the corresponding probe signal of the sheet which carries a fraction $I_i/I$ of the total electrode current $I \sim 1$ MA. Additional information on the Y, $(\Delta t)$s correlation coefficients is reported in Ref. [2] of this Appendix.
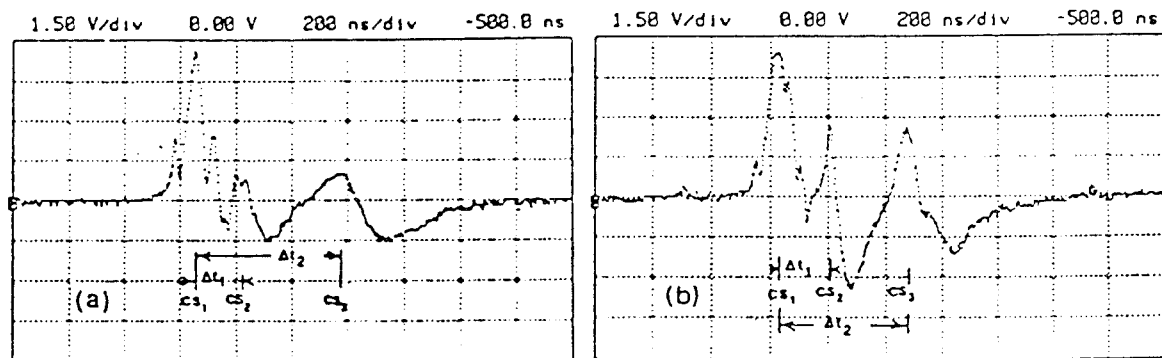


Fig. 1.   P-1 magnetic probe signals from two discharges under the same conditions (W = 18 kJ, p = 6 Torr of pure $D_2$). Y = 0.35 $\bar{Y}$ in (a); Y = 0.9 $\bar{Y}$ in (b).

## References

[1] . H. K. Hartline, F. Ratliff: *Studies in Excitation and Inhibition in.. etc*, Rockefeller Univ. Press, NewYork 1974. F. Ratliff et al: Proc. U.S. Nat. Acad.Sci., 62, 733 (1969).
[2] . A. Bortolotti , J. Brzosko, P. De Chiara, H. Kilic, F. Mezzetti, V. Nardi, C. Powell: Pr. 19-th EPS Conf. Contr. Fusion and Plasma Phys. (Innsbruck, 1992), Vol. 16C, p. 695.

Current Distribution. The radial current $J_r$ is determined from the magnetic probe signal of the time variation $\dot{B}_\theta$ ($\sim J_r$)) of the azimuthal magnetic field between the electrodes /1/. For the discharges (> 90% of the total) in which a multiplicity of current sheaths form we determine the bearing on Y (D+D reactions) of the time spacing $\Delta T$ between the first two current sheaths. Two current sheaths are considered as time resolved if the $\dot{B}_\theta$ signal changes sign between the two leading contiguous peaks, both with the same amplitude sign. Fig. 1(A) reports the PF geometry and the location of the $\dot{B}_\theta$ probes and of the CR-39 targets on which $D^+$ tracks are etched. The values of the linear correlation coefficient r for (Y,$\Delta T$) from different groups of N discharges under different pressure and voltage conditions, are reported in Table I-A. These data were obtained from two identical machines PF(I) and PF(II) with the above PF-1 characteristics and clearly indicate that the smaller is the time spacing $\Delta T$ between leading current sheaths, the higher is the fusion yield Y. The value of r and its confidence level, 1-P(r,N), are affected by the capacitance coupling of the probes with the plasma via boiled-off material from the pyrex case of the probes, a pyrex capillarly tube of 3 mm to 4 mm in diameter. The determination of this capacitance coupling and of its bearing on the $\dot{B}_\theta$ signal from the inductive coupling was carried out with two probes in the same pyrex case. The two identical probes (each with a 1.2 mm diameter loop, and an anti-inductive shielded connection to the H.P. signal monitor) have opposite orientations. The two Fig. 1(B) signals from these two probes of opposite-orientation had a different amplitude reduction [x1/10-for (a); x1/12.5 for (b)] before entering the H.P. digitizer/display system. Consistently, the maximum amplitude Max $\Delta V(+)$ of the leading composite peak 1 in (a), is higher by a factor 1.25 than the absolute amlplitude of peak 1 in (b). This means that no plasma/probe capacitance coupling is affecting the $\dot{B}_\theta$ signal for at least the first 100 ns from the time $t_o$ the leading current sheath starts to sweep the probe. The trailing current signal has a peak 2 with absolute value in (b) equal to that of 2 in (a). This means that the plasma/probe capacitance coupling is a function of time, with an appreciable contribution to the probe signal of about 25% of its amplitude at the time $t_o$ + 230 ns of the peak 2. A conclusion is that for single-probe data, the value of r and of its confidence level 1-P can be modified by rotating the plane of the probe loop by $180^o$. The probe 3 of Table I is the same as probe 2, but for a $180^o$ rotation of the probe loop. The corresponding

data are consistent with the above conclusion and provide an assessment of the capacitance coupling effect on r. The overvoltage surges and restrikes at the PF breech from the resistive surge [of amplitude I$\dot{L}$(plasma)] of the radially imploding current sheath are the direct cause of the dip of absolute value Max $\Delta V(-)$ in the $\dot{B}_\theta$ signal between peaks 1 and 2 of Fig. 1-B. Table I-B reports the linear correlation coefficient (and its confidence level) for Y, Max $\Delta V/\bar{\Delta}V$, where Max $\Delta V$ = Max $\Delta V(+)$ + Max $\Delta V(-)$ and $\bar{\Delta}V$ is the mean value of Max $\Delta V$ for all discharges at the same voltage. This is consistent with the view that a too high velocity of radial implosion of the leading current sheath (note position of probe) will induce, via the voltage surge of amplitude $\dot{L}I$, a detrimental restrike at the breech which crowbars the pinch. We also find that the correlation coefficient for the number of peaks $\nu(\dot{I})$ in the $|dI/dt|$ signal and that $\nu(\dot{B})$ of the $\dot{B}$ signal from the same discharge, in a series of N discharges is $\gamma$ = 0.32 with 1-P(r,N) = 90%. The time spacing between peak of the $\dot{B}_\theta$ signal is systematically smaller than the time spacing between corresponding peaks of the dI/dt signal of the same discharge. This indicates that the trailing current sheaths after rolling-off the interelectrode gap, may linger from 45 ns to about 150 ns in the region after the probe before pinching on the axis.

Contact Prints. Fragments of the PF curreent sheaths are forwardly ejected in the axial direction from the pinch region after the pinch disintegration. A CR-39 target (T) is axially located at a distance D (10 cm or 25 cm) from the end of the positive center electrode, with orientation orthogonal to the elextrode axis. A mylar foil of thickness 50 $\mu$m (or 25 $\mu$m thick, in other tests) covers the T-surface and screens out all D$^+$ ions of energy E < 2.5 MeV (or E < 1.5 MeV). The mylar screen is in contact with the target surface. In some of the tests the screen at the target edges has some spacing, $\bar{d}$, from the target surface to control the loss of sharpness of the plasmoid (contact print) image as a function $\bar{d}$. There the distance $\bar{d}$ between screen and target is < 1 mm. The contact print of the impinging current sheath fragment (or plasmoid) with sharply-defined boundaries is formed from the non-uniform distribution of etched D-tracks on the CR-39 surface. Optical photographs of the plasmoid image formed on the CR-39 ions with E > 2 MeV are reported in Fig. 2 (D = 10 cm). Equally sharp images are obtained for D = 25 cm with both 50 $\mu$m or 25 $\mu$m thick screens. A clear plamoid contact

print is not formed in all discharges. Table 2 summarizes the results from 120 discharges. Each target (5 cm x 10 cm) is exposed to only a single shot. A new screen is used for each target even though no detectable damage was observed on the screen after the exposure. If N(C.P.) is the number of discharges in which a contact print is formed, out of N (Total) discharges under the same conditions, we find that the occurrence ratio R = N (C.P.)/N(Total) with the 25/50 μm screen does not appreciably depend on the PF filling pressure P in the interval 3 Torr $\leq$ P $\leq$ 8 Torr. With the 50 μm screen we also find that R does not depend on D in the interval D = 10 cm/25 cm. The majority of the contact prints from > 2.5 MeV ions shows clearly the same filamentary structure and a similar hot spot abundance in the pinch as we have previously described in the literature/3/. Contact prints are formed independently on the Y(D+D) value of a discharge reaction yield. In the last column at right (of Table II) we indicate the range of the Y values (in terms of the mean value $\bar{Y}$) for the set of discharges (at one pressure value) which exhibit the broadest range.

Nuclear Reactivity. The nuclear reactivity data of Fig 2 have been obtained by following the same method we have reported in /2/. The data provide further confirmation of the hot spot structure of the pinch, and of the concentration of the nuclear fusion reactions in these regions of high density. A lower bound for the density in the hot spots was and is set at $10^{22}$ cm$^{-3}$. The MeV-deuteron induced radioactivity (β+) in the plasma were measured when the PF chamber was filled with deuterium and doped with HZ-nuclei (carbon or nitrogen): This method can differentiate fusion reactivity and spectral characteristics for low energy ions, E $\leq$ 0.1 MeV (D+D fusion), medium energy ions, 0.5 MeV < E < 3 MeV (HZ+D reactions)/2/. The results are assessed in terms of high-reactivity plasma domains (hot-spots). Fig. 2 reports the high-Z fusion reaction yield per discharge $Y_p$ (from D+HZ nuclei) in (a), total fluence $\phi_d$ of fast ions (E > 0.5 MeV) ejected from the pinch in (b), ratio of the radioactivity A of two nuclear reactions (D + 0, D + B) induced from the D-ion bombardment of an azimuthally-symmetric target - in (c) - covering the solid angle 0 $\leq$ $\gamma$ $\leq$ 2π, 25° $\leq$ ר $\leq$ 120°, as functions of the D+D fusion yield, Y, in

the same discharge.  The numerical factor 6.5 in (b) accounts for the different values of the geometry-dependent efficiency of the detectors and of the cross-sections of the two fusion reactions.

$$k = \rho_{HZ}\, \rho_d / (\rho_{dZ} + \rho_d) \text{ in (a); } \quad r = (d\phi_d/dE)\cdot\sigma\ (E)$$

in (c).  $\rho_{HZ},\, j/\rho_{HZ} + \rho_d$ are the density ($cm^{-3}$) of HZ and D nuclei, respectively, in the PF filling gas.

References.

1.  V. Nardi, et al, IEEE Transactions of Plasma Science, Vol. 16, 3, p. 368, 1988.

2.  J. Brzosko & V. Nardi, Physics Letters A, Vol. 155, p. 162, 1991.

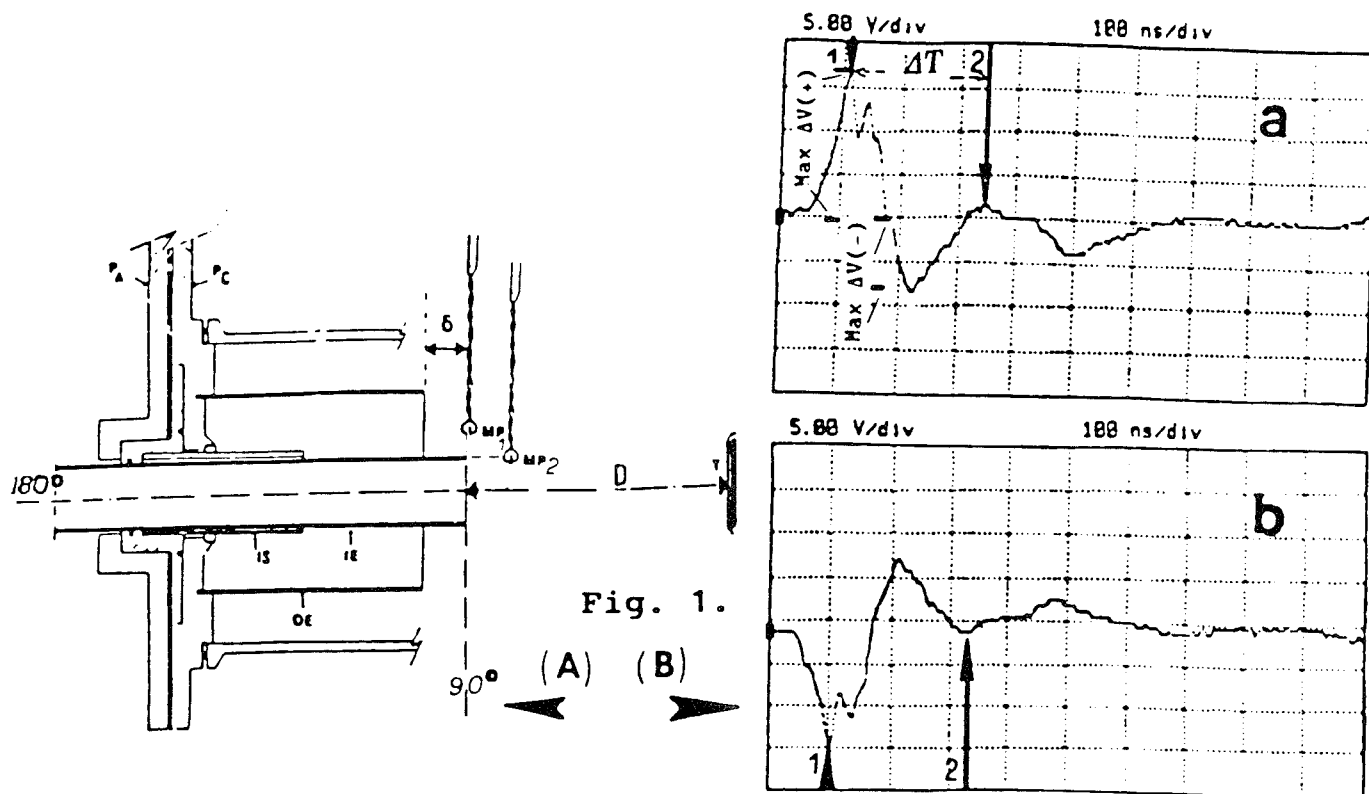3.  W. H. Bostick, et al, J. Plasma Physics, Vol. 8, p. 7, 1972. Nuclear Fusion, Vol. 3, 109 (1974).

Fig. 1 Schematic view of PF, magnetic probes $MP_1$, $MP_2$ and target $T$ in (A). $MP_1$ signal of two probes with opposite orientation, inside the same pyrex case, in (B).

TABLE 2 CONTACT PRINT OF CURRENT SHEATH FRAGMENTS VIA ETCHED ION TRACKS, ON CR-39 TARGETS (TARGET EXPOSED TO A SINGLE DISCHARGE)

| TARGET DISTANCE D (CM) | FILLING PRESSURE (TORR) | MYLAR SCREEN THICKNESS ($\mu M$) AND E | OCCURRENCE RATIO: N(C.P.)/N(TOT.) 16 KV DISCHARGES | | |
|---|---|---|---|---|---|
| 10 | $3 \leq P \leq 8$ | 25 (E>1.5 MEV) | 9/13 | (69%) | $Y(6)=(0.4$ TO $1.6)\bar{Y}(6)$ |
| | | 50 (E>2.5 MEV) | 5/53 | (9%) | $Y(5)=(0.2$ TO $1.8)\bar{Y}(5)$ |
| 25 | $3 \leq P \leq 5$ | 50 (E>2.5 MEV) | 4/25 | (16%) | $Y(4)=(0.9$ TO $1.1)\bar{Y}(4)$ |
| | $5 \leq P \leq 7$ | 50 (E>2.5 MEV) | 3/25 | (12%) | $Y(7)=(0.6$ TO $1.5)\bar{Y}(7)$ |

All data on plasmoid contact prints reported here were obtained from W = 5 kJ PF [similar results were obtained from PF (2)].
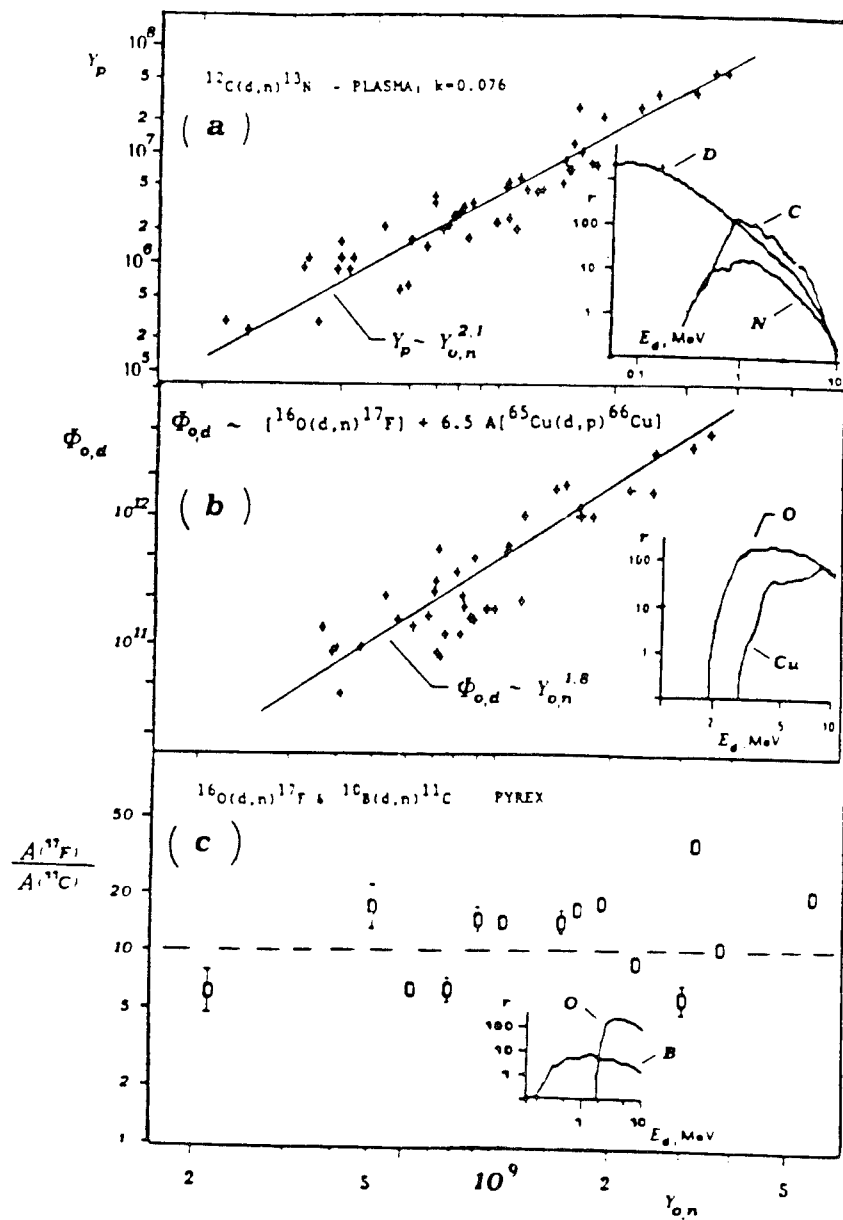
Fig. 2 High-Z reaction yield $Y_p$ in (a), fluence $\Phi_d$ of $D^+$ ions with energy > 0.5 MeV in (b), induced activity ratio on external targets in (c), as a function of the neutron yield (from D+D reactions) from the same PF discharge.

22

# Appendix II

### SCHLIEREN OF CURRENT SHEATH AND PINCH

The experiment with a 10% decrease of magnetic insulation at the breech were carried out with a 6 kJ plasma focus machine (Mather geometry). The dynamics of discharges in deuterium at the filling pressure of 5 torr was monitored also with schlieren photography.

The assembled schlieren optical system consisted of a ruby laser as a source of light, two lenses with a spatial filter forming a Keppler type expander of the laser beam, a schlieren lens with a circular stop, and a camera. The experimental set-up is specified as follows:

---

**Field of view:** The field diameter is 40 mm. The center is located on the electrode axis, 14 mm from the front end of the inner electrode.

**Magnification** (image to object linear size ratio): 1.01

**Resolution,** measured at the set position of photographic plate: $\theta = 30$ μm, i.e., $\theta^{-1} = 33$ line pairs/mm.

**Depth of Field, measured:** The translation of a test object along the beam by $\pm$ 16 mm (about the radius of the inner electrode) changes the resolution from 30 μm to 175 μm (33 lp/mm to 5.7 lp/mm, respectively).

**Sensitivity** (the ratio of electron density gradient integrated along a path –

to the off-axis displacement at the stop): $2.5 \cdot 10^{18}$ cm$^{-3}$/mm.

**Threshold** value (minimum value) of the integral of the density gradient along the beam path, for having a corresponding angular deflection $\Delta\theta$ of the beam wide enough to graze the stop-disc edge and to contribute to the schlieren image ($\Delta\theta$ is determined as the sum of the beam spot radius, 0.7 mm, at the stop, and the stop radius, 1.2 mm): $4.9 \cdot 10^{18}$ cm$^{-3}$.

**The range of electron density gradient** integrated along the beam path $\int (dn_e/dx)\, dy$, forming the image can be selected within $4.9 \cdot 10^{18}$ cm$^{-3}$ and, $1 \cdot 10^{20}$ cm$^{-3}$.

**Source of light:** Ruby laser, Q-switched with a Pockels cell. Wavelength: 694.3 nm. Nominal energy: 1J. Pulse duration FWHM from 10 to 40 ns. Diameter of ruby rod: 9.5 mm: Laser beam divergence: 10 mrad.
Image recorded on Kodak high speed film (developed to contrast index of about 1.7).

---

The schlieren pictures were taken in the time range from t = - 307 ns to t = + 340 ns (± 10 ns), with t = 0 coincident with the sharp peak in the electrode current signal |dI/dt|. For each picture the circuit current derivative, the instant of exposure, the wave-form of the laser beam pulse, and the neutron yield were monitored. Four pictures are presented in Fig. 7 as an example of typical density gradient patterns, directly related to the configuration of the plasma current sheath. A data summary is presented in Table II.
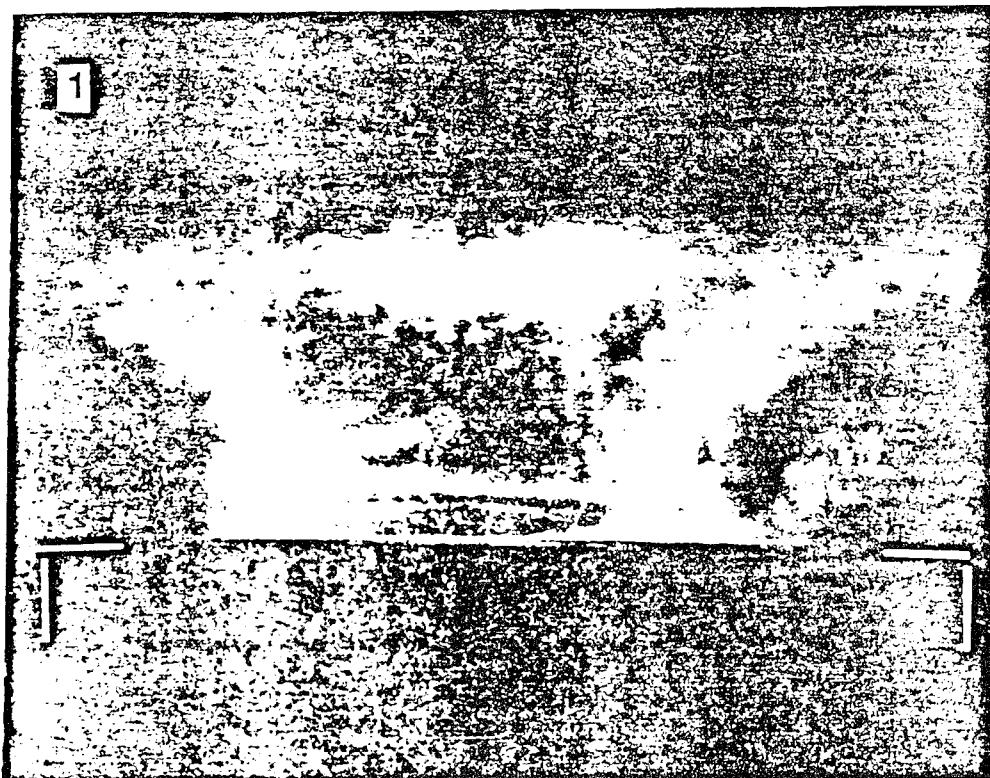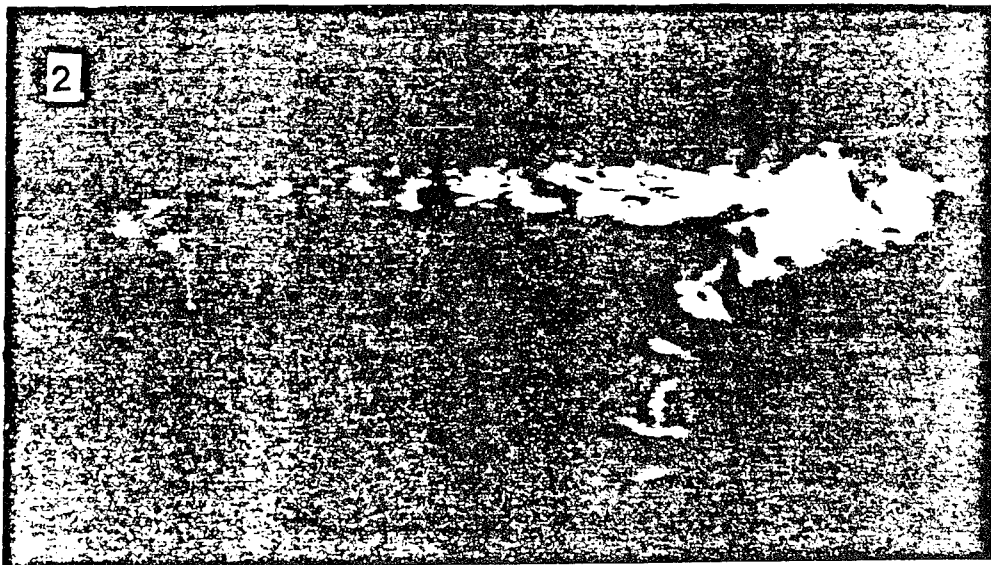
TABLE II. SCHLIEREN DATA.

| Figure:<br>PF discharge No: | 7-1<br>921220-165 | 7-2<br>921223-181 | 7-3<br>921231-200 | 7-4<br>921231-201 |
|---|---|---|---|---|
| Exposure* at the time t = | -92 ns | -47 ns | -42 ns | -34 ns |
| FWHM of laser pulse $\Delta t$ | 25 ns | 20 ns | 36 ns | 35 ns |
| Stop diameter, mm | 2.4 | 10 | 10 | 10 |
| Range of $\int dn_e/dx\,dy$ [$cm^{-3}$] | $5.8\cdot10^{18}$–$1\cdot10^{20}$ | $2.5\cdot10^{19}$–$1\cdot10^{20}$ | $2.5\cdot10^{19}$–$1\cdot10^{20}$ | $2.5\cdot10^{19}$–$1\cdot10^{20}$ |
| Neutron yield | $4.0\cdot10^8$ | $1.9\cdot10^8$ | $1.1\cdot10^9$ | $1.7\cdot10^8$ |

(*THE INDICATED TIME t OF EXPOSURE IS THE TIME OF THE LASER PULSE PEAK)
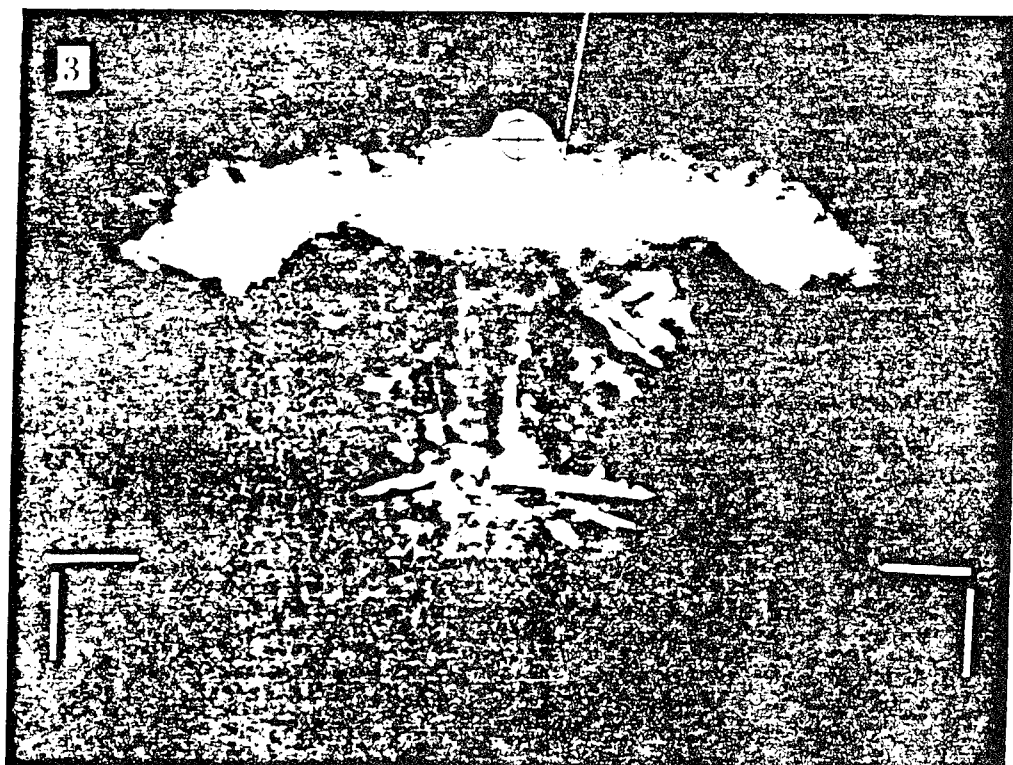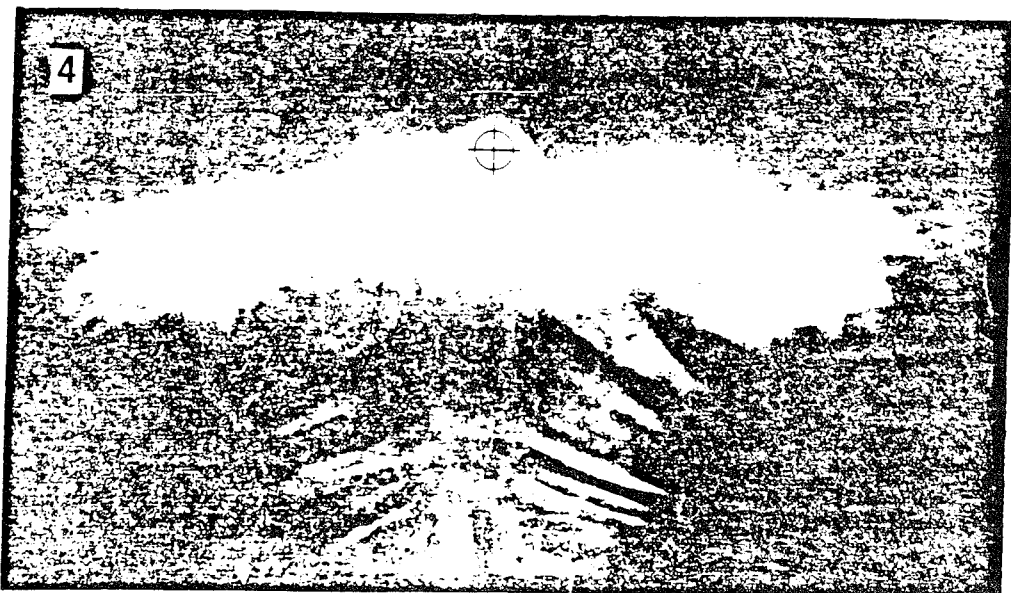
The range of electron density gradient integrated along the beam path was selected by changing the stop diameter. With the stop diameter of 2.4 mm the values of the gradient integral contributing to the image (Fig. 7.1 picture), were in the range from $5.85\cdot10^{18}cm^{-3}$ to $1\cdot10^{20}$ $cm^{-3}$ while with the stop diameter of 10 mm the contributing values were limited to the range from $2.5\cdot10^{19}$ $cm^{-3}$ to $1\cdot10^{20}cm^{-3}$. The pictures taken with a greater-radius stop reveal the current sheath fine structure better than schlieren with a smaller-radius stop because (a), the details of the greater-stop-corresponding image are not masked by contributions from low gradient points of the object (plasma); (b), the details of the fine structure are associated with, and characterized by, high density gradients. Figure 7-2 reports a similar pattern as in Fig. 7-1, with a better-resolved fine structure because of the greater-size stop. Figures 7-3 and 7-4 show a similar "herring-bone" fine-structure of the PF pinch, in spite of the difference in neutron yield by an order of magnitude (these two schlieren pictures have essentially the same exposure instant t, and duration $\Delta t$; the estimated error on t is - 10 ns). We note that the fine structure is not smeared, and that the straight lines of the "herring-bone" pattern are almost the same in the two pictures. Turbulence with formation of circular loops is observed in the image of the discharge with the highest neutron pulse (Fig. 7-3).

The schlieren images can be used for estimating the average (over space and over the time $\Delta t$) of the x-component of the electron density gradient,

$\Delta n / \Delta x$, along the laser beam path (y axis) of estimated length $\Delta y$ across the plasma (essentially equal to the chord of the current sheath circular cross-section on a plane orthogonal to the electrode axis z), with the result: $\Delta n / \Delta x = (4 \pm 2) \cdot 10^{19} \text{ cm}^{-4}$ ($\Delta y \cong 3$ mm) in (1) and $\Delta n / \Delta x = (1.3 \pm 0.7) \cdot 10^{20} \text{ cm}^{-4}$ in (2). The average value $\Delta n / \Delta x = (3 \pm 1.5) \cdot 10^{20} \text{ cm}^{-4}$ is obtained at a later time, $t > -42$ ns, over the compressed-pinch cord of length $\Delta y \cong 1.7$ mm at $t \cong 0$, in (3,4). At earlier times (e.g. $t \lesssim -40$ ns), the apparent width D of the image luminous band of high density gradient moving with the current sheath (D = 3-4 mm), is essentially determined by the relatively-long exposure (with velocity-induced smearing effect). Consistently, we can estimate the average radial velocity $v_r$ of the current sheath, during the interval ($-104$ ns, $-80$ ns) as $v_r = D / \Delta t \cong 1.2 \cdot 10^7$ cm/s. This value agree, within about 10%, with the radial-velocity determination from magnetic probe data [3]. Alternatively, from the probe-measured velocity ($v_r \cong 1.1 \cdot 10^7$ cm/s) we determine the current sheath thickness, $\delta$, where the density gradient is localized, via $\delta = D - v_r \cdot \Delta t$ ($\delta = 1.0 \pm 0.5$ mm). As an independent method for determining $\delta$ and $\Delta y$, we also use the laser capability of generating two or three laser pulses during one PF discharge. From the corresponding multiple current-sheath images on the same schlieren frame, we then obtain the velocity $v_r$, the sheath velocity-induced smearing of the current sheath profile, where the high values of the density gradient are localized, and the separation of $\delta$ from D.

34   mm

34　mm